



# DNS in evolution of vorticity and sign relationship in wake transition of a circular cylinder: (pure) mode A

L. M. Lin<sup>1</sup> · Z. R. Tan<sup>2,3</sup>

Received: 25 April 2019 / Revised: 4 June 2019 / Accepted: 28 June 2019 / Published online: 22 August 2019

© The Chinese Society of Theoretical and Applied Mechanics and Springer-Verlag GmbH Germany, part of Springer Nature 2019

## Abstract

In the present paper, the spatio-temporal evolution of vorticity in the first wake instability, i.e., (pure) mode A, is investigated in order to understand the wake vortex dynamics and sign relationships among vorticity components. Direct numerical simulation (DNS) for the flow past a circular cylinder is performed, typically at a Reynolds number of 200, in the three-dimensional (3-D) wake transition. According to characteristics of time histories of fluid forces, three different stages are identified as the computational transition, the initial stage and fully developed wake. In the second initial stage, the original two-dimensional spanwise vortices become obviously three-dimensional associated with the streamwise or vertical vorticity intensified up to about 0.1. As a matter of fact, these additional vorticities, caused by the intrinsic 3-D instability, are already generated firstly on cylinder surfaces early in the computational transition, indicating that the three-dimensionality appeared early near the cylinder. The evolution of additional components of vorticity with features the same as mode A shows that (pure) mode A can be already formed in the late computational transition. Through careful analysis of the vorticity field on the front surface, in the shear layers and near wake at typical times, two sign laws are obtained. They illustrate intrinsic relationships among three vorticity components, irrelevant to the wavelength or Fourier mode and Reynolds number in (pure) mode A. Most importantly, the origin of streamwise vortices is found and explained by a new physical mechanism based on the theory of vortex-induced vortex. As a result, the whole process of formation and shedding vortices with these vorticities is firstly and completely illustrated. Other characteristics are presented in detail.

**Keywords** Wake transition · Circular cylinder · Vorticity · Mode A · Sign law

## 1 Introduction

Bluff bodies are widely used in many engineering applications, such as suspension bridges, high architecture, flexible risers and pipelines in offshore oil platforms, and heat exchangers. Flow past a bluff body is a classical and basic subject in fluid mechanics. One main reason is the appearance of unsteady wake associated with vortices alternately shed behind a body. As a result, the generated large unsteady fluid

forces acted on a body have the potential to lead to fatigue damage and even violently destroy the structural integrity of a body. With the aim of understanding and controlling the wake vortex dynamics, a large number of studies [1–15] have been published in recent decades by applying many methods, including physical model testing, direct numerical simulation (DNS), and linear or non-linear stability analysis. Comprehensive reviews on such subjects can be found in previous references [4, 11].

Based on these investigations for flow past a circular cylinder [4], four laminar stages for different flow structures in the wake mainly appear in a wake transition sequence. In the laminar steady regime at a Reynolds number  $Re$  below around 49, where  $Re$  is defined based on the approaching flow velocity  $U_\infty$ , the cylinder diameter  $D$  and the kinematic viscosity  $\nu$  of the fluid, the wake comprises a steady recirculation region of two symmetrically placed vortices on each side of the wake. After the primary wake instability emerges at  $Re > 49$  due to a Hopf bifurcation, the

✉ Z. R. Tan  
1084341511@qq.com

<sup>1</sup> Key Laboratory for Mechanics in Fluid Solid Coupling Systems, Institute of Mechanics, Chinese Academy of Sciences, Beijing 100190, China

<sup>2</sup> School of Navigation, Wuhan University of Technology, Wuhan 430063, China

<sup>3</sup> Hubei Key Laboratory of Inland Shipping Technology, Wuhan University of Technology, Wuhan 430063, China

two-dimensional (2-D) spanwise vortices (with spanwise vorticity  $\omega_z$ ) are alternately shed from the body, known as Kármán vortex streets, in the laminar vortex shedding regime at  $Re < 140$ –194. Until the Reynolds number reaches about 260, two discontinuous changes, mainly associated with two wake instabilities, i.e., modes A and B, in the wake formation appear in the three-dimensional (3-D) laminar wake transition regime. Beyond a Reynolds number of 260 in the last stage, a particularly ordered 3-D streamwise vortex structure (with streamwise vorticity  $\omega_x$ ) in the near wake, the fine-scale three-dimensionality, becomes increasingly disordered, while the primary wake instability behaves remarkably like the laminar shedding mode.

Particularly, in the 3-D wake-transition regime, two different wake instabilities, typically manifested by the variation of Strouhal number  $St$  (non-dimensional vortex-shedding frequency) as  $Re$  is increased, appear successively with their specific mechanisms and features [4,7,8,10,14]. At the first discontinuity, which is hysteretic near  $Re = 180$ –194, the first wake instability, i.e., (pure) mode A, occurs with the inception of vortex loops due to the spanwise wavy deformation of primary vortices as they are shed. Such deformation is caused by an elliptic instability of the primary vortex cores and the formation of streamwise vortex pairs at a spanwise wavelength of around 3–4 diameters are resulted from Biot–Savart induction. At the second discontinuous change in the  $St$ – $Re$  relation over a range of  $Re$  from 230 to 250, the second wake instability, i.e., (pure) mode B, gradually appears due to a gradual transfer of energy from mode A shedding. Mode B comprises finer-scale streamwise vortices, with a spanwise length scale of around one diameter. It is mainly due to a hyperbolic instability of the braid shear layer region.

Except above two pure modes, there is a large intermittent low-frequency wake velocity fluctuation due to the presence of large-scale spot-like vortex dislocations in the wake transition with mode A, i.e., mode A\* (mode A + vortex dislocations) [4]. The critical Reynolds number  $Re_{cr}$  at which mode A\* wake instability emerges is identified at 194 through careful experiments, in which the end effects are eliminated by using non-mechanical end conditions [5]. This value is very close to those of  $188.5 \pm 1.0$ ,  $190 \pm 0.02$  and  $190.5$  predicted through linear stability analysis [3,11,12]. In addition, the effect of mode A\* instability would destabilize mode B in the nonlinear interaction between the two modes [6]. This leads to the first emergence of mode B instability at  $Re$  about 230 in experiments [5] much lower than the critical  $Re$  of 259 and  $261 \pm 0.2$  predicted through linear stability analysis [3,11], but in good agreement with predicted  $Re = 230$  based on nonlinear stability analysis [9,13]. Moreover, the experimental study has revealed that the wake transition from mode A\* to mode B is a gradual process with intermittent swapping between the two modes [5]. Therefore, the appearance

of mode A\* or vortex dislocations will seriously interfere both pure modes A and B in the 3-D wake transition of a circular cylinder.

As for (pure) modes A and B, there are two distinct features for spatial distributions of streamwise vortices and primary Kármán vortices. For mode A, most of the streamwise vorticity comes from vorticity initially pulled out of the primary vortex core into the vortex braid region during shedding. The stretching thereafter occurs in a manner similar to the strong straining near the braid saddle point in the mixing layer [16], as the basic streamwise interaction between streamwise and spanwise vortices. Therefore, the strain-rate field leads to the spanwise vortex becoming highly deformed across the span. However, the instability of mode B does not appear to be related to a waviness of the primary vortex as in mode A, because these vortices deform much more uniformly along their length. Furthermore, these two modes have distinct symmetries. Mode A comprises streamwise vortices of one sign that are in a staggered arrangement from one braid region to the next, whereas mode B has an in-line arrangement of streamwise vortices of the same sign. These patterns are intimately linked to the fact that streamwise vortices formed in a previous half-cycle are in the vicinity of newly forming streamwise vortices [4].

A central question pertains to the effect of vertical vortices (with vertical vorticity  $\omega_y$ ) on (pure) modes A and B, even vortex dislocation, in the 3-D wake transition of a bluff body, which is seldom investigated in previous literature. Typically, as reported in a previous work [17], the strong vertical vorticity in the near wake, associated with the weak streamwise vorticity, plays a key role in the complete suppression of Kármán vortices by introducing a certain conic disturbance on the circular cylinder at  $Re = 100$ . This indicates another basic interaction, referred to as the vertical interaction between vertical and spanwise vortices [18]. In most cases, these two types of basic interactions (streamwise and vertical interactions) all lead to the original spanwise vortices wavy varied across the span, and consequently different vortex-shedding patterns appearing in the near wake of the cylinder with geometrical disturbances. Interestingly, it has been shown that two sign laws of vorticity, as an intrinsic relationship of vorticity between two basic interactions, appear in the spatial evolution of vorticity in the near wake of such bluff body [18] and theoretically confirmed by the theory of vortex-induced vortex (VIVor) in a recent study [19]. Therefore, it is still not totally understood for the role of the vertical vorticity or vortex in the vorticity evolution in the near wake of a circular cylinder without any geometric disturbance, even the origin of streamwise or vertical vorticity in the 3-D wake-transition process, from the point of investigating vorticity sign.

In light of these earlier works, there are two primary aims in present study, as the first part. One is to investigate the

spatial-temporal evolution of vorticity, particularly including the vertical vorticity, and sign relationship in the first natural wake instability mode, i.e., pure mode A, for a flow past a circular cylinder by means of DNS. Another is to find the physical origin of streamwise vorticity in the shear layers in mode A. Mode B and large-scale vortex dislocation will be reported in the future. To avoid the contamination of large-scale vortex dislocations, pure mode A is investigated, typically at  $Re = 200$ . Only one spanwise wavelength of four diameters is taken into account, near the most unstable wavelength [4,6]. The rest of this paper is organized in the following manner. The governing equations coupled boundary conditions and numerical methods are firstly presented. Then, based on time histories of fluid forces, different features in the spatio-temporal evolution of vorticity in different stages, including the appearance of  $\omega_x$  and  $\omega_y$ , the intrinsic sign relationship of vorticity and the key effect of  $\omega_y$  on the origin of streamwise and vertical vortices are mainly investigated and discussed in detail. Finally, conclusions are obtained.

## 2 Physical model

### 2.1 Governing equations

As shown in Fig. 1a, the fluid flow past a still circular-section cylinder with diameter  $D$  is studied. The flow is incompressible with a constant density  $\rho$  and kinematic viscosity  $\nu$  of the fluid. The inertial Cartesian coordinate system is established as shown in Fig. 1a, where the  $x$  axis (streamwise direction) is aligned to the incoming free stream with uniform velocity  $U_\infty$ , the  $z$  axis (spanwise direction) is parallel to the cylinder span, and the  $y$  axis (vertical direction) is normal to the free stream and the cylinder axis.

The incompressible continuity and Navier–Stokes equations without any conservative body forces in dimensionless form are written by

$$\nabla \cdot \mathbf{u} = 0, \quad (1)$$

$$\frac{\partial \mathbf{u}}{\partial t} + (\mathbf{u} \cdot \nabla) \mathbf{u} = -\nabla p + \frac{1}{Re} \nabla^2 \mathbf{u}, \quad (2)$$

where  $\nabla$  is the gradient operator,  $\mathbf{u}$  is the velocity vector with three components ( $u, v, w$ ) along their own coordinates,  $t$  is the time scaled by  $D/U_\infty$ ,  $p$  is the static pressure scaled by  $\rho U_\infty^2$ ,  $Re$  is defined as  $U_\infty D/\nu$ . The velocities are scaled by the free-stream velocity  $U_\infty$  and lengths by the cylinder diameter  $D$ . Thus, all variables used in the following context are scaled by  $\rho, U_\infty$  and  $D$ . In the spatial-temporal evolution of vorticity and vortex dynamics in the bluff body wake, the main control parameter is the Reynolds number. The vorticity  $\boldsymbol{\omega}$  is defined as the curl of velocity  $\mathbf{u}$ , i.e.,  $\boldsymbol{\omega} = \nabla \times \mathbf{u}$ , with three components ( $\omega_x, \omega_y, \omega_z$ ) along their own coordinates, which are governed by the following vorticity transport equation,

$$\frac{\partial \boldsymbol{\omega}}{\partial t} + (\mathbf{u} \cdot \nabla) \boldsymbol{\omega} = (\boldsymbol{\omega} \cdot \nabla) \mathbf{u} + \frac{1}{Re} \nabla^2 \boldsymbol{\omega}. \quad (3)$$

As an important indicator in the present flow dynamics, variations of drag and lift forces,  $F_D$  and  $F_L$ , acting on the body are taken account of and normalized as the drag and lift coefficients,  $C_D$  and  $C_L$ , respectively, defined by

$$C_D = \frac{F_D}{\frac{1}{2} \rho U_\infty^2 S}, \quad C_L = \frac{F_L}{\frac{1}{2} \rho U_\infty^2 S}, \quad (4)$$

where  $S$  is the projected area of cylinder along the free stream direction. Then the mean drag coefficient,  $\overline{C_D}$ , and the root-mean-square (RMS) lift coefficient,  $C'_L$ , are defined by

$$\overline{C_D} = \frac{1}{N} \sum_{i=1}^N C_{Di}, \quad C'_L = \sqrt{\frac{1}{N} \sum_{i=1}^N (C_{Li} - \overline{C_L})^2}, \quad (5)$$

where  $N$  is the number of values in the time history of  $C_D$  or  $C_L$ , and  $\overline{C_L}$  is the time-averaged lift coefficient with definition similar to  $\overline{C_D}$ . When spanwise vortices are alternately

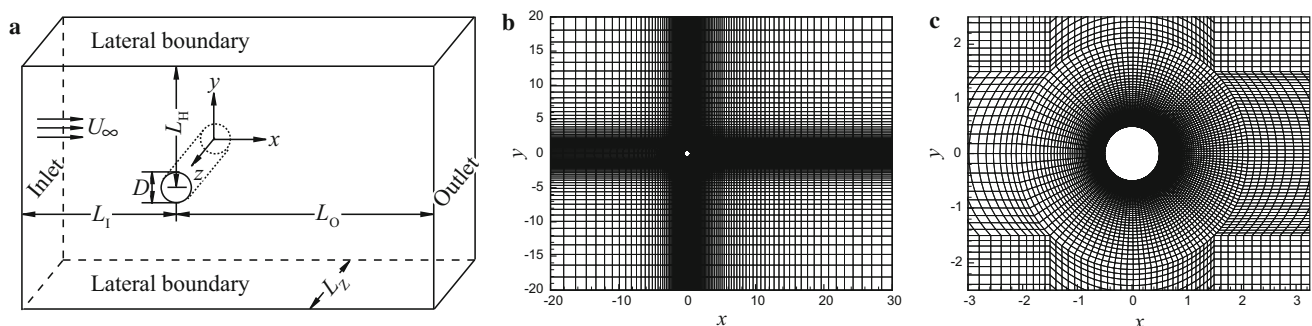


**Fig. 1** a Schematics of flow past a straight cylinder with the circular cross-section, and computational domain in the  $(x, y)$  plane and mesh distributions **b** in the whole flow region and **c** near the cylinder with a closer view

shed in the near wake, the frequency of such vortex shedding,  $f$ , is obtained through the Fourier analysis of the time history of  $C_L$ , and scaled as the Strouhal number  $St = fD/U_\infty$ .

## 2.2 Initial and boundary conditions

As for initial conditions, the flow is assumed to be still with  $\mathbf{u} = \mathbf{0}$  and  $p = 0$  at  $t = 0$ , except at the inlet.

As for boundary conditions, the 3-D flow is assumed to be spatially periodic across the span. At the inlet, a uniform free stream is prescribed as  $u = U_\infty$  and  $v = w = 0$ . At the outlet, the simple outflow with  $\partial \mathbf{u} / \partial x = \mathbf{0}$  is applied. At both lateral boundaries in the vertical direction, the symmetry boundary condition, i.e., free slip with velocity  $\frac{\partial u}{\partial y} = v = \frac{\partial w}{\partial y} = 0$ , is adopted. On cylinder surfaces, the non-slip boundary condition with  $\mathbf{u} = \mathbf{0}$  is used. The reference pressure,  $p_\infty = 0$ , is specified at center of inlet.

## 2.3 Computational domain and mesh

The whole computational domain for present wake flow is shown in Fig. 1a. Along with the  $x$  axis, the inlet length,  $L_I$ , defined as the distance between the cylinder center and inlet boundary, is 20, and the outlet length,  $L_O$ , defined as the distance from the cylinder center to the outlet boundary, is 30, while the vertical height,  $L_H$ , defined as the distance between the lateral boundary and the cylinder center along the  $y$  axis, is 20. The blockage ratio, defined by  $1/(2L_H)$ , is, therefore, 2.5%. Along the  $z$  axis, the computational spanwise length or the cylinder span,  $L_Z$ , defined as the distance between two spanwise periodic boundaries across the span, is 4 for  $Re = 200$ , the same as one instability wavelength for mode A. Correspondingly, the whole computational domain in dimensionless form is  $(20 + 30) \times (20 + 20) \times 4$  or  $50 \times 40 \times 4$  in cubic space of  $x \times y \times z$ .

The mesh distribution in the whole 2-D computational domain is presented in Fig. 1b, as the standard mesh applied for the present computations. As for the mesh resolution, the smallest grid size of 0.001 is the normal distance of the first layer of mesh next to the cylinder surface. A local mesh is mainly refined in the big circular region with a radial diameter of about 4.24, as shown in Fig. 1c. A coarse mesh is mainly distributed far away from the cylinder. The cell expansion ratio at the wake center plane  $y = 0$  is 1.11 near the incoming flow, 1.06 around the cylinder and 1.05 near the far wake. Therefore, the total number of present 2-D standard mesh (SM) is 20,100.

Under the present circumstances with the periodical flow across the span, the uniform spanwise grid size,  $\Delta z$ , is closely related to not only the computational resolution, but also the flow dynamics. To better understand it, let us transform the problem of determining  $\Delta z$  in physical space

into that of solving the  $n$ -th wavenumber  $\beta_n = 2\pi n/L_Z$  in spectral space. In Eq. (2), the spanwise viscous item,  $\frac{1}{Re} \frac{\partial^2 \mathbf{u}}{\partial z^2}$ , can be expressed by a sum of Fourier modes,  $\frac{1}{Re} \sum \beta_n^2 \hat{\mathbf{u}}_n e^{i\beta_n z}$ , where  $\hat{\mathbf{u}}_n(t, x, y)$  is the  $n$ -th spanwise Fourier mode of  $\mathbf{u}(t, x, y, z)$  and  $n \geq 0$ . Therefore, viscous dissipation becomes important at wavenumbers  $\beta_D \sim Re^{\frac{1}{2}}$ . At wavenumbers  $\beta_n > \beta_D$  the momentum equations are dominated by viscous forces [6]. These high-wavenumber modes contribute little to the dynamics of the flow at large scales because their energy is rapidly dissipated by viscosity. For an adequate description of the dynamics in a system with a given spanwise dimension  $L_Z$  we only need a finite set of  $N$  Fourier modes to cover the range of scales from  $\beta_0 = 0$  (the mean flow) to  $\beta_D = 2\pi N/L_Z \sim Re^{\frac{1}{2}}$ , or  $N \sim L_Z Re^{\frac{1}{2}}/(2\pi)$ . Corresponding to physical space, the computational spanwise size  $\Delta z$  is just equivalent to  $L_Z/(2N)$  due to symmetries, associated with the spectral resolution at the smallest dissipation wavelength  $\lambda_D = L_Z/N$ . In present computational spanwise domain, we have  $N \approx 9$  and  $\Delta z \approx 0.22$  ( $\lambda_D \approx 0.44$ ) for  $L_Z = 4$  at  $Re = 200$ . Therefore, we just investigate the 3-D flow dynamics with spanwise periodicity at the smallest periodic resolution of  $\Delta z = 0.1$  in present paper.

## 2.4 Numerical methods

Numerical calculations are carried out by a widely used commercial software FLUENT V6.3.26 with the finite-volume method (FVM). Adopting the FVM coupled with spanwise periodic boundary conditions is physically attributed to the non-periodic vortex structure possibly disappearing near the mid-span [14] if the spanwise spectral method is applied, or only symmetrical wake flow with the symmetry boundary condition of Neumann type across the span [20], respectively. The pressure-implicit with splitting of operators (PISO) as the pressure–velocity coupling scheme is applied. The pressure equation is solved by the second-order discretization scheme. The momentum equation adopts the second-order upwind scheme. Particularly, the Green–Gauss node-based method is applied for the gradient computation.

All unsteady formulations are solved by using the second-order implicit scheme. The dimensionless time step  $\Delta t$  is 0.01. In the present computations at  $Re = 200$ , the maximum of cell Courant number,  $Co = \Delta t |u| / \Delta l$ , is less than approximately 0.8, where  $\Delta l$  is the cell size in the direction of the local velocity  $u$  through a cell.

Error of mass conservative equation, Eq. (1), reaches magnitude on the order of as low as  $O(10^{-5})$ , while errors of three components of momentum equations, Eq. (2), are lower at around an order of  $O(10^{-7})$  in all computations.



**Table 1** Comparisons of hydrodynamic parameters,  $\overline{C_D}$ ,  $C'_L$  and  $St$ , among different computational domains (SM, LSM and SSM), mesh resolutions (SM, MS and MW) and the smallest grid sizes (SM, SMG2 and SMG5) in the present 2-D numerical simulations at  $Re = 250$ 

Cases	$\overline{C_D}$	$C'_L$	$St$
SM	1.3486	0.5586	0.2029
LSM	1.3402	0.5541	0.2023
SSM	1.3826	0.5752	0.2065
MS	1.3451	0.5551	0.2021
MW	1.3572	0.5560	0.2046
SMG2	1.3500	0.5687	0.2023
SMG5	1.3520	0.5720	0.2015

## 2.5 Model verifications

The present numerical model is firstly validated with the simulation results of 2-D wake flow with SM at  $Re$  from 46 to 49 with an interval of 1. The unsteadiness of 2-D flow appears at  $Re = 47$ , but vanishes at  $Re = 46$ , determined by the lift force gradually amplified or not, which is consistent with numerical results [6,11] and close to  $Re = 49$  in experiment [4].

The independence study of 2-D computational domain in  $(x, y)$  plane is carried out at  $Re = 250$  with almost same mesh resolution, as shown in Table 1. Among them, the computational domain in the 2-D SM is  $(20 + 30) \times (20 + 20) = 50 \times 40$ . While the large standard mesh (LSM) is  $(30 + 40) \times (30 + 30) = 70 \times 60$ , and the small standard mesh (SSM) is  $(10 + 20) \times (10 + 10) = 30 \times 20$ . The relative error of hydrodynamic parameters between SM and LSM is less than 1%, while that for SM and SSM is about 2%–4%. This demonstrates that the present computational domain, SM, is suitable for DNS.

Then, the mesh dependence is also studied at  $Re = 250$  with different 2-D mesh resolutions, as shown in Table 1. Among them, the cell number around the cylinder surface is doubled as 260, and the total number of grids in such modified mesh on surface (MS) is 35,400. Moreover, the grid number in the wake,  $x \in (2.12, 30]$ , is also doubled as 100 with the cell expansion ratio reduced to 1.015. Consequently, the total number of cells in this refined mesh in the wake (MW) is 25,600. It is found out that the relative error is less than 1% among three different meshes.

Moreover, the independence of the smallest grid size on the cylinder surface is investigated at  $Re = 250$ , as shown in Table 1 for SM, SMG2 and SMG5. Among them, the smallest grid size is 0.002 in the mesh SMG2 and increased up to 0.005 in the mesh SMG5 without change of total grid numbers. As the smallest grid size increases, the fluid forces are gradually increased, while the vortex-shedding frequency is reduced. Except that the mean drag force and  $St$ , only the

**Table 2** Hydrodynamic parameters,  $\overline{C_D}$ ,  $C'_L$  and  $St$ , in the present 2-D numerical simulations at  $Re = 200, 250$  and  $300$ , where Num1 and Num2 are numerical results of Refs. [11] and [14], respectively

$Re$	Cases	$\overline{C_D}$	$C'_L$	$St$
200	SM	1.3329	0.4695	0.1946
	Num1	1.3283	0.4756	0.1949
	Num2	1.3427	0.4724	0.1966
250	SM	1.3486	0.5586	0.2029
	Num1	1.3459	–	0.2028
	Num2	1.361	0.5658	0.2047
300	SM	1.3651	0.6297	0.2091
	Num2	1.3768	0.6407	0.2107

lift force is varied greatly and the relative error exceeds 1%. Therefore, the smallest grid size is very important in present DNS, especially in capturing main characteristics of vorticity and its sign evolved near the cylinder surface.

Finally, the verifications based on the 2-D standard mesh are also carried out at  $Re = 200, 250$  and  $300$ , respectively, and compared with previous numerical results, as presented in Table 2. The relative errors are less than 2%. In these 2-D calculations, the frequency resolution  $\delta f$  is  $8.3 \times 10^{-4}$ , associated with the computational time period of about 1200 after spanwise vortices are alternately shed steadily with the almost constant peak-amplitude of lift coefficient.

The following analysis is mainly performed at  $Re = 200$ . However, as a part of the independence study, the effect of Reynolds number, i.e.,  $Re = 190, 195$  and  $210$ , on relationship of vorticity sign, and the effect of spanwise grid size,  $\Delta z = 0.05$ , on the 3-D vortex evolution at  $Re = 200$  are also investigated and presented at last.

## 3 Results and discussion

### 3.1 Time histories of fluid forces and frequency analysis

Above all, let us present the characteristics of time histories of the drag and lift coefficients, as shown in Fig. 2. Before the 3-D wake flow with (pure) mode A at  $Re = 200$  is fully developed with peak-amplitudes of drag and lift coefficients little wavy varied at  $t > 380$  in Fig. 2b, two different stages are identified. The first is a computational transition at  $t < 70$ , as shown in Fig. 2a. The second is an initial stage of 3-D wake flow over the range of time,  $70 < t < 380$ , as shown in Fig. 2b.

In the computational transition (CT),  $t < 70$ , there are four stages with obviously different characteristics of drag and lift coefficients in Fig. 2a. The first stage (CT-1) at  $t < 0.6$  is just corresponding to the non-physical oscillations of fluid

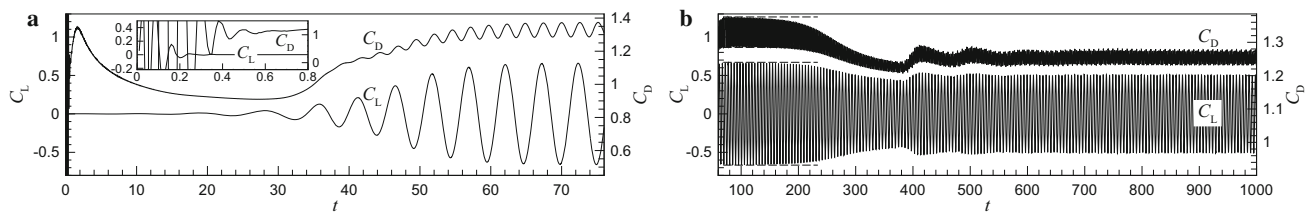


**Fig. 2** Time histories of the drag and lift coefficients,  $C_D$  and  $C_L$ , for (pure) mode A at  $Re = 200$ , typically **a** the computational transition,  $t \in (0, 70)$ , with a small window at  $t < 0.8$ , **b** the initial stage,  $t \in (70, 380)$ , and the fully developed stage,  $t > 380$ . In **b**, the horizontal dashed lines denote the peak-to-peak amplitudes of  $C_D$  and  $C_L$  at the first initial stage with almost 2-D spanwise vortices

forces. They are caused by the inconsistent initial conditions between the still flow in an interior flow region and the free stream flow at inlet for  $t = 0$ , and rapidly reduced as time proceeds. Then in the second stage (CT-2) for  $0.6 < t < 1.7$ , the drag coefficient increases up to the local maximum, but the lift coefficient is always zero. When the time increases from 1.7 up to 28 in the third stage (CT-3), the drag coefficient is gradually reduced down to the local minimum, while the oscillating amplitude of lift coefficient is slowly increased when  $t > 10$ . Subsequently, in the last stage (CT-4) at  $28 < t < 70$ ,  $C_D$  is also gradually increased and oscillated at  $t > 40$ , associated with the continual increasing of oscillating amplitudes of  $C_L$ .

During the initial stage (IS),  $70 < t < 380$ , two phases, quasi-periodic 2-D flow and initially developed 3-D flow, are clearly demonstrated by temporal variations of fluid forces in Fig. 2b. As for quasi-periodic 2-D flow stage (IS-1) in a range of time,  $t \in (70, 140-180)$ , the oscillated amplitudes of drag and lift coefficients are almost invariant with the time. And we have  $\overline{C_D} = 1.3288$ ,  $C'_L = 0.4629$  and  $St = 0.1923$  ( $\delta f = 9.2 \times 10^{-3}$ ), a little less than those in 2-D computations in Table 2. However, for gradually developed 3-D flow stage (IS-2) at  $140-180 < t < 380$ , the peak-to-peak amplitudes of fluid forces are quickly reduced, almost linearly for  $C_L$  or nonlinearly for  $C_D$ , respectively.

For the fully developed wake (FDW) with (pure) mode A at  $t \in (380, 1000)$ , as shown in Fig. 2b, two phases successively appear. The first (FDW-1) is the wavy variation of peak-to-peak amplitudes of fluid forces in a time range between 380 and 600. The second (FDW-2) is almost constant of such amplitudes when  $t > 600$ . Particularly in FDW-2, there are  $\overline{C_D} = 1.2545$ ,  $C'_L = 0.3569$ , and  $St = 0.1802$  with  $\delta f = 2.8 \times 10^{-3}$ , in a good agreement with  $\overline{C_D} = 1.2412$ ,  $C'_L = 0.3556$ , and  $St = 0.1815$  in a previous work [11]. On the other hand,  $St$  in present mode A is really less than that in 2-D calculations in Table 2, which fits very well with dependency study of Strouhal number on the periodicity length [11].

Through the Morlet wavelet analysis for  $C_L(t)$ , different temporal features of the vortex-shedding frequencies could be obtained. As shown in Fig. 3 with a time range from 20 to

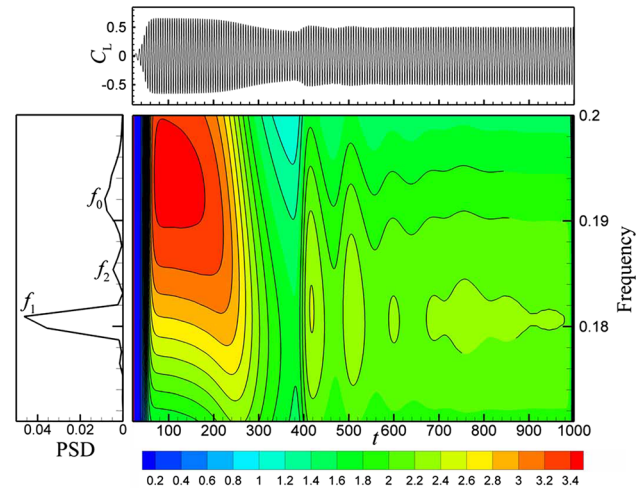


**Fig. 3** Frequency spectra of  $C_L$  through the Morlet wavelet analysis at  $Re = 200$  with two basic frequencies,  $f_0 = 0.192$  and  $f_1 = 0.1809$ , and a mixed frequency,  $f_2 = 0.1854$ , at the frequency resolution of  $\delta f = 1.1 \times 10^{-3}$  from 20 to 1000. PSD means power spectra density

1000, there are two basic frequencies identified,  $f_0 = 0.192$  and  $f_1 = 0.1809$ , associated with (almost) 2-D flow in the first initial stage (IS-1) and the fully developed 3-D wake flow, respectively. Between them, i.e., IS-2, there is a mixed frequency,  $f_2 = 0.1854$ , based on  $f_0$  and  $f_1$ , because of  $f_2 \approx \frac{1}{2}(f_0 + f_1)$  within the frequency resolution of  $\delta f = 1.1 \times 10^{-3}$ .

### 3.2 Evolution of vorticity and its sign relationship

In the present contexts, spatial distributions of vorticity field at different typical times are analyzed. Three sub-regions are mainly concerned: the boundary layer on and near the front surface (R-I), the separated shear layers beside the body (R-II) and the near wake behind the body (R-III), similar to those in previous work [19]. Local regions on the rear surface and in the recirculation near wake center plane (WCP) will be investigated in the future. In iso-surfaces and contours of vorticity, in order to avoid a possible contamination or interference caused by computational errors, additional

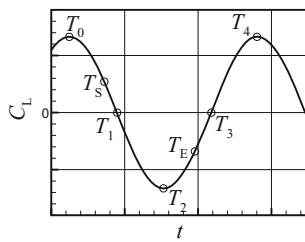


**Fig. 4** Typical points in a whole period or cycle of oscillated lift coefficient, where  $T_0$  (or  $T_4$ ) and  $T_2$  denote the positive and negative extremum values of lift force, respectively, and both  $T_1$  and  $T_3$  are associated with  $C_L = 0$ ,  $T_S$  and  $T_E$  are related to the formation of streamwise and vertical components of vorticity in the shear layers in (pure) mode A

vorticities,  $\omega_x$  and  $\omega_y$ , are only presented with magnitudes at least 0.001, i.e.,  $|\omega| \geq 0.001$ .

From the point of illuminating specific signs of dominant additional vorticities with non-zero value,  $\omega$ , it is frequently used by a sign function,  $\text{sgn}(\omega)$ , defined by

$$\text{sgn}(\omega) = \begin{cases} 1, & \text{if } \omega > 0, \\ -1, & \text{if } \omega < 0. \end{cases} \quad (6)$$

As for spacial position, the streamwise position on and near the front surface is denoted by  $x < 0$ , while that on and near the rear surface, in the shear layers and near wake is denoted by  $x > 0$ . The vertical positions on the upside and downside of cylinder surfaces are denoted by  $y > 0$  and  $y < 0$ , respectively.  $y > 0$  and  $y < 0$  can also be used to denote the upper and lower shear layers and upper and lower sides of WCP, where shedding spanwise vortices with negative and positive signs are correspondingly dominant, respectively.

In addition, it should be stated here that special moments are selected at a time interval of 0.5, equal to that of saved data, because of the limited disk space. Typically,  $T_0$  (or  $T_4$ ) and  $T_2$ , as shown in Fig. 4, are mainly selected to illustrate the vorticity field, associated with a certain variation of lift force. For example, the presented time  $t$ , associated to a certain lift coefficient at  $T_i$  ( $i=0-4$ ), indicates that  $t$  is approximately equal to  $T_i$  within the half time interval of 0.25, i.e.,  $|t - T_i| < 0.25$ .

### 3.2.1 In the computational transition

There is a paucity literature about the spatio-temporal evolution of vorticity reported in such computational transition. To illustrate two sign laws [19] irrelevant to the time, we select some typical moments to show vorticity evolution, as well as in the initial stage and fully developed wake. The first stage (CT-1) is not presented due to its non-physical reason mentioned before. For other three stages, typically as shown in Fig. 5 at  $t = 1$  and Fig. 6 at  $t = 1.5$  in the second stage

(CT-2), Fig. 7 at  $t = 10$  and Fig. 8 at  $t = 27.5$  in the third stage (CT-3), and Fig. 9 at  $t = 49$  in the last transitional stage (CT-4), spacial distributions of (dominant)  $\omega_x$  and  $\omega_y$ , as well as  $\omega_z$ , are analyzed.

In general, the vortex structure in present wake flow is firstly described by a pair of spanwise vortices symmetrically attached on rear surface at  $t = 1$  (Fig. 5c), and gradually elongated downstream till  $t = 10$  (Fig. 7c). Such attached spanwise vortex pair and elongated both upper and lower shear layers become asymmetrically oscillated a little at  $t = 27.5$  (Fig. 8c). Finally in CT-4, these attached spanwise vortices are alternately shed from the upper and lower shear layers, i.e., the formation of Kármán vortex streets, e.g. at  $t = 49$  (Fig. 9c). At least, they always seem to be two-dimensional without any obviously wavy disturbance across the span.

The main feature is the appearance of additional components of vorticity,  $\omega_x$  and  $\omega_y$ . As for the most important information provided in the present stage, additional vorticities with very small magnitudes are firstly generated on the cylinder surface early in CT-2, then convected downstream into the shear layers due to the nonlinear convection, and finally dissipate owing to the viscous forces during CT-2 and CT-3, or alternately shed in CT-4. Moreover, these additional vorticities on the surface and in the shear layers gradually increase as time progresses in CT-3 and CT-4. They are associated with the spanwise flow ( $w \neq 0$ ) first appearing and then increasing near cylinder walls due to the intrinsic 3-D instability, similar to experimental results [21,22]. This clearly indicates that the flow is actually already three-dimensional early in stage of CT-2. In addition, the magnitude of  $\omega_x$  and  $\omega_y$  increased up to about 0.02 still has no effect on 2-D spanwise vortices.

Evolution of Fourier mode is presented by counting the number of vorticity with one pair of positive and negative signs along the spanwise direction. In the computational transition, it seems that in CT-2, the mode of  $n = 1$  (the wavelength  $\lambda$  about 4) mainly appears on and near the front surface, while the mode of  $n \approx 4$  ( $\lambda \approx 1$ ) dominantly exists on and behind the rear surface, according to the spatial distribution of  $\omega_x$  or  $\omega_y$ , typically, as shown in Fig. 5a, b. In CT-3 and CT-4, the Fourier mode of  $n = 4$  totally disappears, while the mode of  $n = 1$  quickly grows and dominates. The latter with  $\lambda = 4$ , exactly equal to the wavelength of (pure) mode A  $\lambda_A = 4$ , indicates that the instability of mode A could initially occur on and near cylinder walls earlier.

Whatever the Fourier mode is, special distributions of vorticity sign is obtained. Firstly, in sub-region R-I, whenever in CT-2, CT-3 and CT-4, the sign of  $\omega_x$  on the upper and front surface, denoted by  $(x < 0, y > 0)$ , is always the same as the sign of  $\omega_y$ . While in sub-regions R-II and R-III ( $x > 0$ ), the sign of  $\omega_x$  is still dominantly the same as the sign of  $\omega_y$  in the upper shear layer ( $y > 0$ ), but opposite in

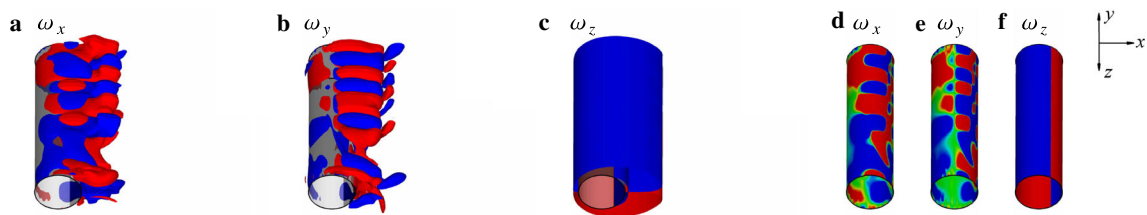


**Fig. 5** At  $t = 1$  (CT-2), iso-surfaces of **a**  $\omega_x = \pm 0.001$ , **b**  $\omega_y = \pm 0.001$  and **c**  $\omega_z = \pm 0.1$ , and contours of **d**  $\omega_x$ , **e**  $\omega_y$  and **f**  $\omega_z$  on cylinder surfaces at  $Re = 200$ , where red and blue colors denote positive and negative values, respectively, and green denotes values almost zero ( $|\omega| < 0.001$ ). Note that the cylinder is denoted by the grey translucent surface in iso-surfaces

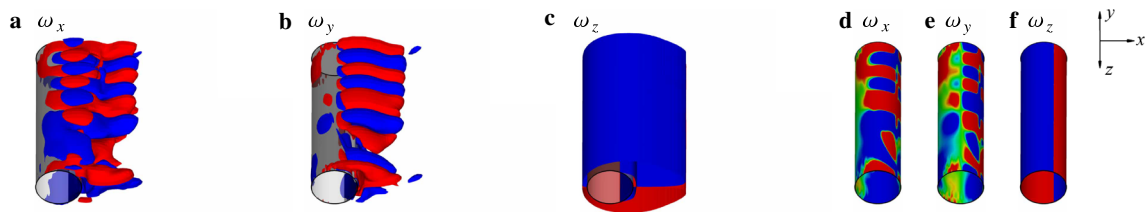


**Fig. 6** At  $t = 1.5$  (CT-2), iso-surfaces of **a**  $\omega_x = \pm 0.001$ , **b**  $\omega_y = \pm 0.001$  and **c**  $\omega_z = \pm 0.1$ , and contours of **d**  $\omega_x$ , **e**  $\omega_y$  and **f**  $\omega_z$  on surfaces at  $Re = 200$  (same descriptions of Fig. 5)

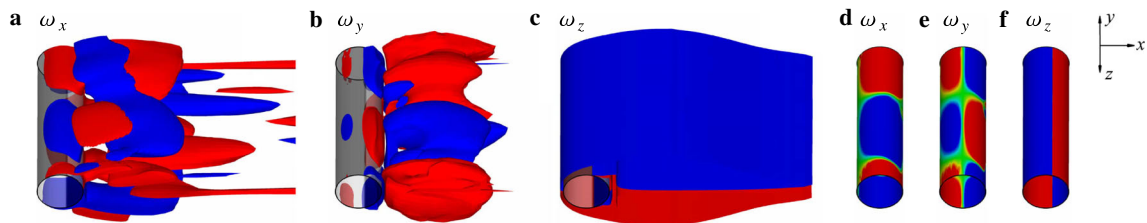


**Fig. 7** At  $t = 10$  (CT-3), iso-surfaces of **a**  $\omega_x = \pm 0.002$ , **b**  $\omega_y = \pm 0.002$  and **c**  $\omega_z = \pm 0.6$ , and contours of **d**  $\omega_x$ , **e**  $\omega_y$  and **f**  $\omega_z$  on surfaces at  $Re = 200$  (same descriptions of Fig. 5)

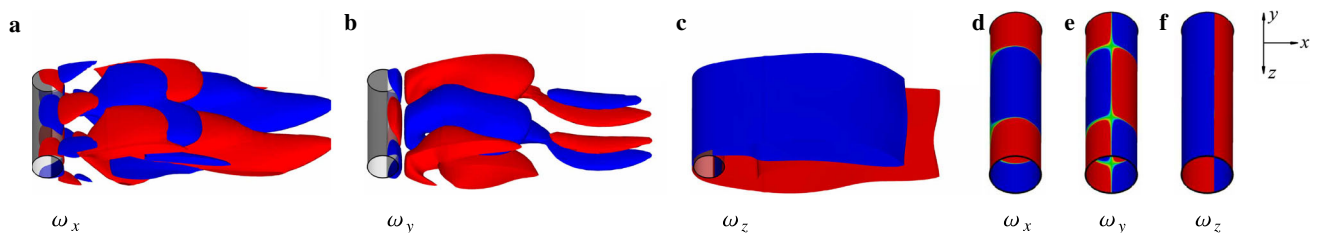


**Fig. 8** At  $t = 27.5$  (CT-3), iso-surfaces of **a**  $\omega_x = \pm 0.02$ , **b**  $\omega_y = \pm 0.02$  and **c**  $\omega_z = \pm 1.0$ , and contours of **d**  $\omega_x$ , **e**  $\omega_y$  and **f**  $\omega_z$  on surfaces at  $Re = 200$  (same descriptions of Fig. 5)

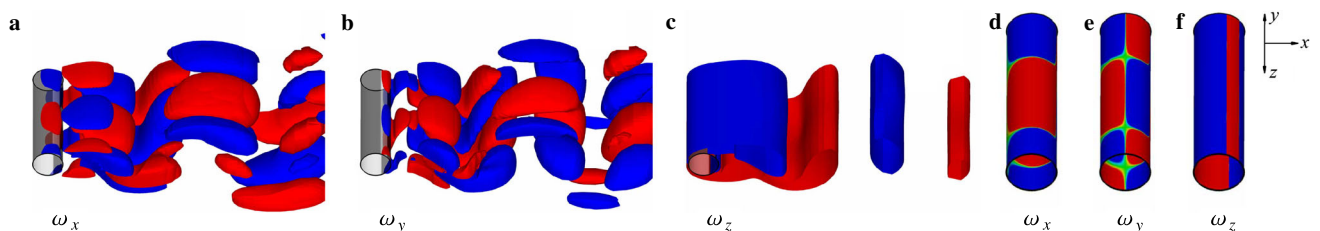


**Fig. 9** At  $t = 49$  (CT-4,  $T_2$ ), iso-surfaces of **a**  $\omega_x = \pm 0.02$ , **b**  $\omega_y = \pm 0.02$  and **c**  $\omega_z = \pm 0.8$ , and contours of **d**  $\omega_x$ , **e**  $\omega_y$  and **f**  $\omega_z$  on surfaces at  $Re = 200$  (same descriptions of Fig. 5)



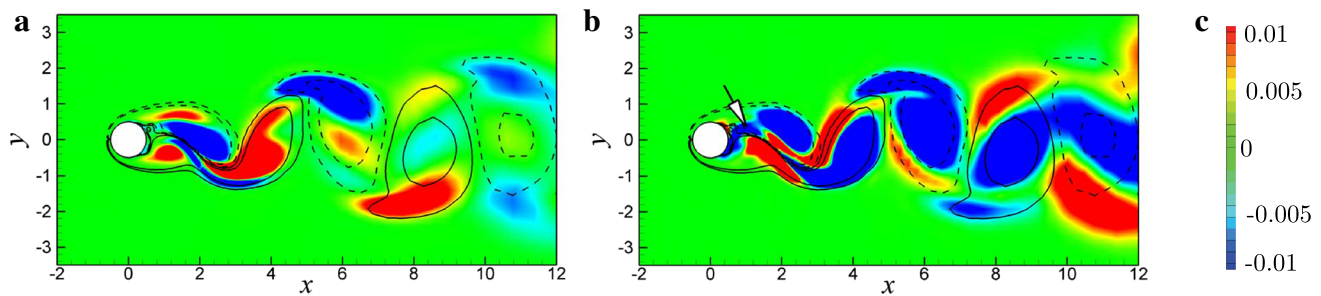


**Fig. 10** Colorful contours of **a**  $\omega_x$  and **b**  $\omega_y$  at  $z = 0.27, t = 49$  (CT-4,  $T_2$ ) and  $Re = 200$ , where red and blue (also shown in **c** color legend just for a reference), as well as solid and dashed contours of  $\omega_z = \pm 0.1$  and  $\pm 0.5$ , denote positive and negative values, respectively. Note that the arrow with a hollow head in **b** denotes  $\omega_y$  in the upper shear layer actually originated from that on the lower and rear surface

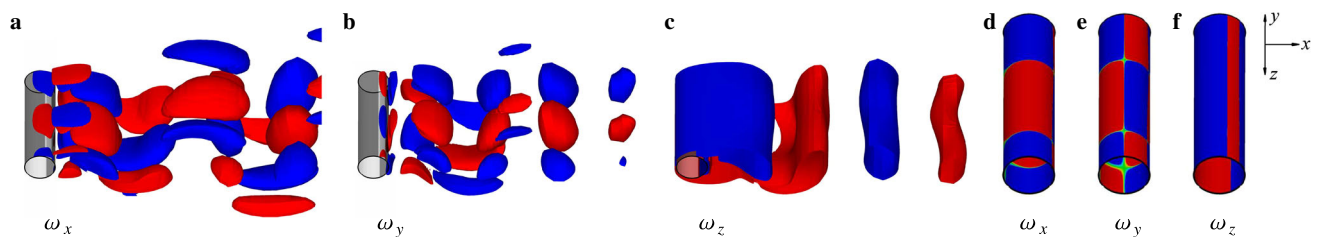


**Fig. 11** At  $t = 173$  (IS-1,  $T_2$ ), iso-surfaces of **a**  $\omega_x = \pm 0.1$ , **b**  $\omega_y = \pm 0.1$  and **c**  $\omega_z = \pm 0.8$ , and contours of **d**  $\omega_x$ , **e**  $\omega_y$  and **f**  $\omega_z$  on surfaces at  $Re = 200$  (same descriptions as Fig. 5)

the lower shear layer ( $y < 0$ ). As a result, it can be reduced to  $\text{sgn}(\omega_x \cdot \omega_y) = 1$  in R-I ( $x < 0, y > 0$ ) and R-II and R-III ( $x > 0, y > 0$ ), and similarly  $\text{sgn}(\omega_x \cdot \omega_y) = -1$  in R-I ( $x < 0, y < 0$ ) and R-II and R-III ( $x > 0, y < 0$ ), referred to as the first sign law. Moreover, the sign of spanwise vorticity on front surface, shear layers and near wake is taken into account, i.e.,  $\text{sgn}(\omega_z) = -1$  at  $y > 0$  and  $\text{sgn}(\omega_z) = 1$  at  $y < 0$ . Then we have an interesting vorticity relationship:  $\text{sgn}(\omega_x \cdot \omega_y \cdot \omega_z) = -1$ , whatever for  $x < 0$  or  $x > 0$  and  $y > 0$  or  $y < 0$ , referred to as the second sign law.

On the other hand, every component of vorticity itself has different spacial distributions. For example, in sub-region R-I, especially in CT-3,  $\text{sgn}(\omega_x)$  at  $y > 0$  is just opposite to that at  $y < 0$ , while  $\text{sgn}(\omega_y)$  at  $x < 0$  is opposite to that at  $x > 0$ , typically, as shown in Fig. 8d, e, respectively. But at  $T_2$  in CT-4 (Fig. 9), the sign of  $\omega_x$  is always the same regardless of whether it is on the upper or lower surface and front or rear surface (except the near wake center), but  $\text{sgn}(\omega_y)$  is almost symmetric about the cylinder center. Meanwhile, in sub-regions of R-II and R-III, e.g. in CT-4, as shown in Fig. 10a, the sign of dominant streamwise vorticity is varied from the upper shear layer to the lower shear layer, and then in both vortex braid regions due to the stretching effect of primary vortex core with an opposite sign, exactly similar to the symmetry of mode A, i.e., a staggered arrangement from one braid region to the next [4]. However, in the same regions, as shown in Fig. 10b, the sign of dominant vertical vorticity is totally the same in both the upper and lower shear layers, similar to that appearing in mode A of a square cylinder [23].

### 3.2.2 In the initial stage

As for the initial stage, the vorticity field in Fig. 11 ( $t = 173$ ) in IS-1 and Fig. 12 ( $t = 375$ ) in IS-2 is analyzed.

In the first stage (IS-1), the shedding spanwise vortices are still almost two-dimensional with a little waviness across the span, although  $\omega_x$  and  $\omega_y$  are continually increased up to about 0.1 as time goes on, as shown in Fig. 11c. These additional vorticities also result in the drag and lift coefficients a little less than those in the 2-D wake flow, as well as a little decrease of vortex-shedding frequency, as mentioned before.

However, in the second initial stage (IS-2), the wake flow is obviously described by the wavy spanwise vorticities. Therefore, it is certainly three-dimensional, even for both the upper and lower shear layers a little wavy along the  $z$  axis. Meanwhile, associated  $\omega_x$  and  $\omega_y$  are increased up to at least 0.2, which leads to remarkable reduction of the peak-to-peak amplitudes of fluid forces over time. Specific distributions of vorticity in the near wake indicate that the (pure) mode A is initially formed in present sub-stage of IS-2, by comparing with those in the subsequent stage, the fully developed wake.

The dominant Fourier mode is relatively complex in different regions. For example, whenever in IS-1 or IS-2, spatial distributions of  $\omega_x$  and  $\omega_y$  with specific signs at the Fourier mode of  $n = 1$  ( $\lambda = \lambda_A = 4$ ) still dominate in the shear layers and near wake, very similar to those in CT-4, while on the front surface, the Fourier mode of  $n = 1$  is still dominant in IS-1. But in IS-2, only on and near cylinder surfaces and just behind the rear surface, e.g. as shown in Fig. 12b, e,

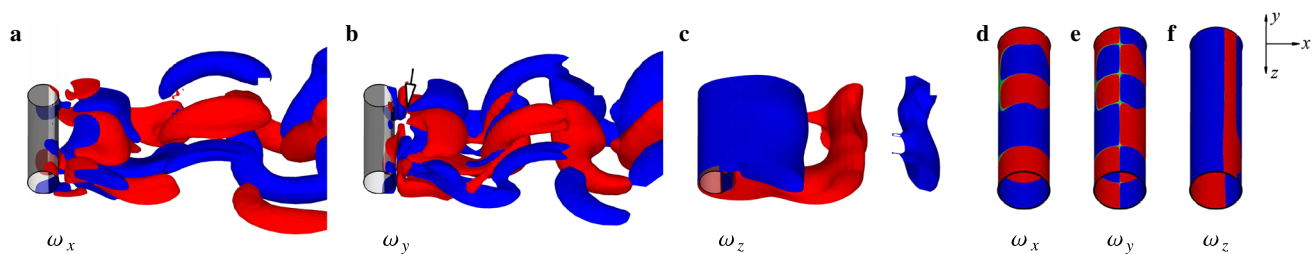


**Fig. 12** At  $t = 375$  (IS-2,  $T_2$ ), iso-surfaces of **a**  $\omega_x = \pm 0.3$ , **b**  $\omega_y = \pm 0.2$  and **c**  $\omega_z = \pm 0.8$ , and contours of **d**  $\omega_x$ , **e**  $\omega_y$  and **f**  $\omega_z$  on surfaces at  $Re = 200$  (same descriptions as Fig. 5). In **b**, the arrow with a hollow head denotes that the vertical vorticity in the upper shear layer originates from that on the rear surface near  $z = 0$

**Table 3** Summary of Fourier mode,  $n = 2$ , appearing on the upper (+y) or lower (-y) surface and the front (-x) or rear (+x) surface in sub-regions IS-2 and FDW at  $Re = 200$

$t$	$(-x, +y)$	$(+x, +y)$	$(-x, -y)$	$(+x, -y)$
307.5 ( $T_2$ )	$n = 2$	$n = 2$	$n = 1$	$n = 2$
375 ( $T_2$ )	$n = 2$	$n = 2$	$n = 1$	$n = 1$
472 ( $T_0$ )	$n = 1$	$n = 2$	$n = 2$	$n = 2$
560.5 ( $T_0$ )	$n = 1$	$n = 2$	$n = 1$	$n = 2$
$T_0$ or $T_4$	$n = 1$	$n = 1$	$n = 1$	$n = 2$

the Fourier mode of  $n = 2$  with  $\lambda \approx 2$  appears. As for only cylinder surfaces, as summarized in Table 3 based on Fig. 13, two groups with different Fourier modes ( $t = 307.5, 375$ ) are identified in the present stage. According to the spacial range of vorticity, at  $t = T_2$ , the mode of  $n = 2$  on the upper surface is obviously stronger than that on the lower surface. This shows multiple Fourier modes coexisting in the natural instability, particularly appearing on and near cylinder surfaces.

Even so, we can still obtain two sign laws in the present initial stage. For example, in sub-region R-I, whenever the Fourier mode of  $n = 2$  is weak or strong,  $\text{sgn}(\omega_x)$  is always the same as  $\text{sgn}(\omega_y)$  at  $y > 0$  but opposite at  $y < 0$ , e.g. in Figs. 12 and 13. This is exactly consistent with that presented in the computational transition. Distributions of  $\omega_x$  and  $\omega_y$  with specific signs are almost synchronously varied with time. Even in sub-regions R-II and R-III with the Fourier mode of  $n = 1$ , such as Figs. 11 and 12, the first sign law still prevails, irrelevant to the shedding spanwise vortices. Mean-

while, for dominant  $\omega_x$  and  $\omega_y$  accompanied with special  $\omega_z$ , the second sign law for three components of vorticity also exists, i.e.,  $\text{sgn}(\omega_x \cdot \omega_y \cdot \omega_z) = -1$ , in sub-regions R-I and R-II. However in R-III, this relationship seems to be invalid. It is mainly attributed to the stretching effect of the upstream spanwise vortex with an opposite sign on the downstream rib-like vortex tubes with  $\omega_x$  and  $\omega_y$ . Particularly, these streamwise vortices are often convected into the upstream spanwise vortex core. For example,  $+|\omega_x|$ , originally shed with  $+|\omega_z|$  in the lower shear layer, is moved into the core of  $-|\omega_z|$  at  $x = 6$  in Fig. 14a.

As for the spacial distributions of additional vorticities on cylinder surfaces, it can be seen that the symmetrical feature in CT-4 is also existed in present IS-1, but totally disappear in IS-2 because of the strong disturbance of Fourier mode of  $n = 2$ .

### 3.2.3 In the fully developed wake

Different typical moments are chosen to show spacial characteristics of the vorticity field when  $t > 380$ . For example, the first stage (FDW-1) is typically shown in Fig. 15 ( $t = 560.5$ ) at which the peak amplitude of lift coefficient is locally minimal. Because cases at times of  $T_0$  and  $T_2$  are not strictly in a whole period in previous analysis for the sake of simplicity, in the second stage (FDW-2), the flow is analyzed in two different half-periods, such as ( $T_0, T_1, T_2$ ) or ( $T_2, T_3, T_4$ ), typically as shown in Fig. 16 at  $t = 872$  ( $T_1$ ) and Fig. 17 at  $t = 873.5$  ( $T_2$ ), or Fig. 18 at  $t = 980$  ( $T_3$ ) and Fig. 19 at  $t = 981.5$  ( $T_4$ ), respectively. Notice that the view in the second half-period is from the bottom to the top of cylinder with

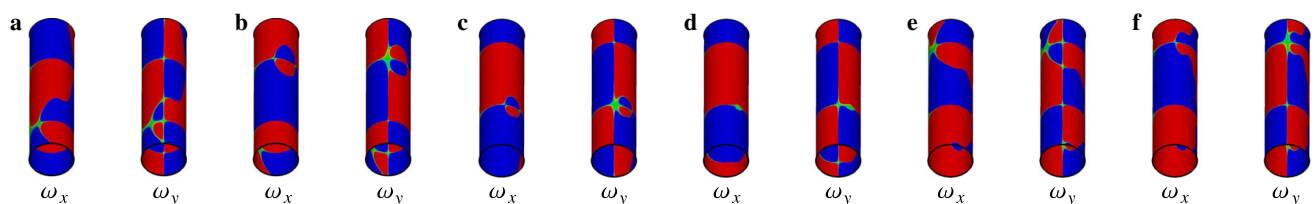


**Fig. 13** At  $Re = 200$ , contours of  $\omega_x$  and  $\omega_y$  at **a**  $t = 307.5$  ( $T_2$ ) and **b**  $472$  ( $T_0$ ) on upper surfaces and **c**  $t = 307.5$  ( $T_2$ ), **d**  $375$  ( $T_2$ ), **e**  $472$  ( $T_0$ ) and **f**  $560.5$  ( $T_0$ ) on lower surfaces viewed from the  $-|y|$  axis (same descriptions as Fig. 5). The flow is from left to right

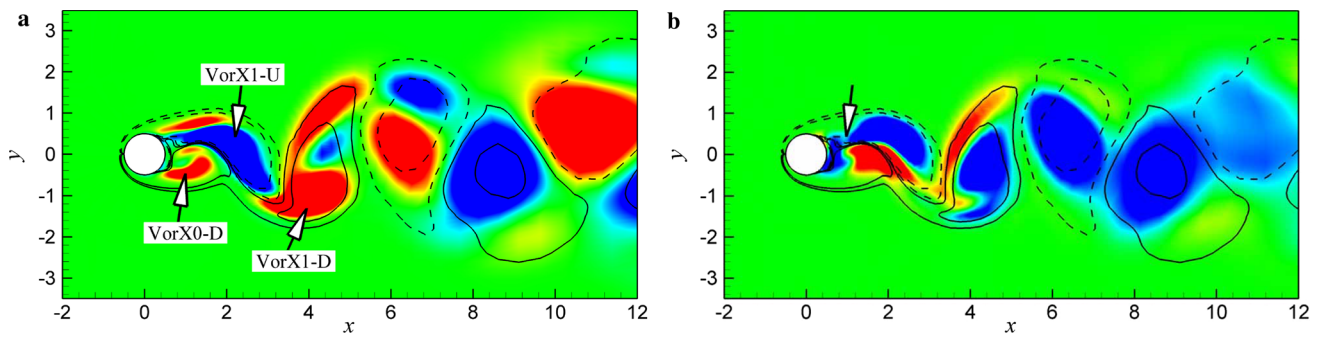


**Fig. 14** Colorful contours of **a**  $\omega_x$  and **b**  $\omega_y$  at  $z = 0.8$ ,  $t = 375$  (IS-2,  $T_2$ ) and  $Re = 200$  (same descriptions as Fig. 10). In **b**, the arrow with a hollow head denotes  $\omega_y$  in the upper shear layer actually originated from that on the lower and rear surface

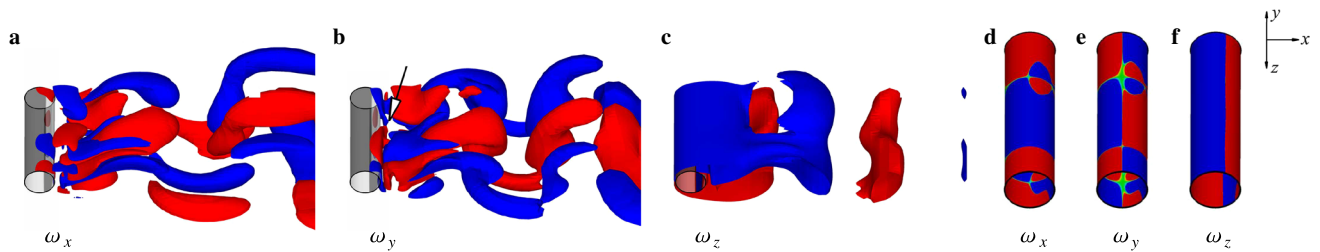


**Fig. 15** At  $t = 560.5$  (FDW-1,  $T_0$ ), iso-surfaces of **a**  $\omega_x = \pm 0.3$ , **b**  $\omega_y = \pm 0.2$  and **c**  $\omega_z = \pm 0.8$ , and contours of **d**  $\omega_x$ , **e**  $\omega_y$  and **f**  $\omega_z$  on surfaces at  $Re = 200$  (same descriptions as Fig. 5). In **b**, the arrow with a hollow head denotes that the vertical vorticity in the lower shear layer originates from that on the upper and rear surface near  $z = 0$

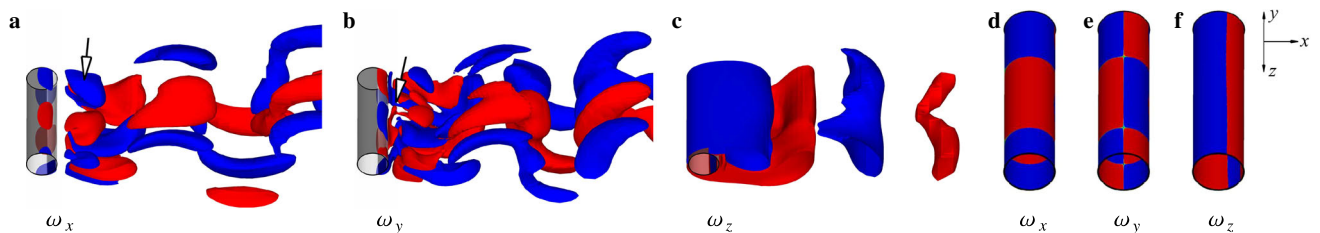


**Fig. 16** At  $t = 872$  (FDW-2,  $T_1$ ), iso-surfaces of **a**  $\omega_x = \pm 0.4$ , **b**  $\omega_y = \pm 0.2$  and **c**  $\omega_z = \pm 0.8$ , and contours of **d**  $\omega_x$ , **e**  $\omega_y$  and **f**  $\omega_z$  on surfaces at  $Re = 200$  (same descriptions as Fig. 5). In **a** and **b**, the arrows near  $z = 0$  denote the increased streamwise vorticity and the vertical vorticity near the upper and rear surface, respectively

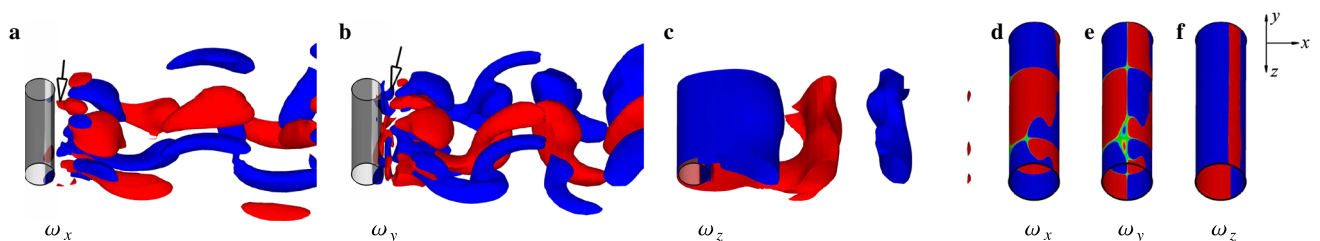


**Fig. 17** At  $t = 873.5$  (FDW-2,  $T_2$ ), iso-surfaces of **a**  $\omega_x = \pm 0.4$ , **b**  $\omega_y = \pm 0.2$  and **c**  $\omega_z = \pm 0.8$ , and contours of **d**  $\omega_x$ , **e**  $\omega_y$  and **f**  $\omega_z$  on surfaces at  $Re = 200$  (same descriptions as Fig. 5). In **a** and **b**, the arrows near  $z = 0$  denote the initially generated streamwise vorticity and the vertical vorticity on the lower and rear surface stretched into upside, respectively

the aim of clearly showing streamwise and vertical vorticity in the lower shear layer.

This clearly shows that the 3-D wake flow is fully developed with the appearance of (pure) mode A. The (pure) mode A is mainly described by alternately shedding spanwise vor-

tices accompanied by a pair of rib-like vortex tubes with streamwise and vertical vorticities at specific signs. In the vortex structure of mode A, the sign of dominant streamwise vorticity in the upper and lower shear layers at the same spanwise position is opposite, indicating streamwise vortices

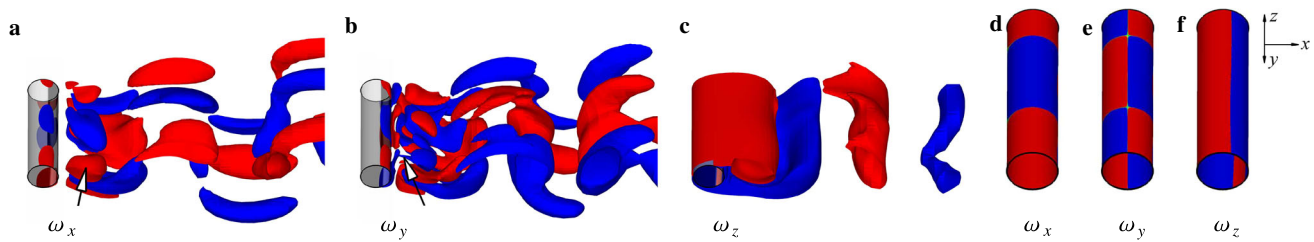


**Fig. 18** At  $t = 980$  (FDW-2,  $T_3$ ), iso-surfaces of **a**  $\omega_x = \pm 0.4$ , **b**  $\omega_y = \pm 0.2$  and **c**  $\omega_z = \pm 0.8$ , and contours of **d**  $\omega_x$ , **e**  $\omega_y$  and **f**  $\omega_z$  on surfaces at  $Re = 200$  (same descriptions as Fig. 5). In **a** and **b**, the arrows near  $z = 0$  denote the increased streamwise vorticity and the vertical vorticity near the lower and rear surface, respectively

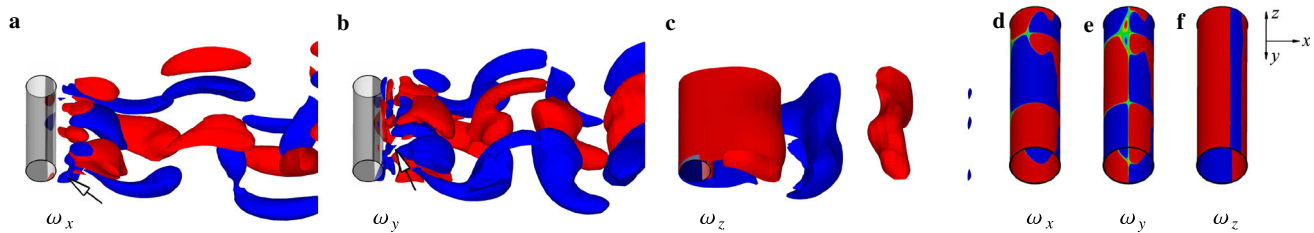


**Fig. 19** At  $t = 981.5$  (FDW-2,  $T_4$ ), iso-surfaces of **a**  $\omega_x = \pm 0.4$ , **b**  $\omega_y = \pm 0.2$  and **c**  $\omega_z = \pm 0.8$ , and contours of **d**  $\omega_x$ , **e**  $\omega_y$  and **f**  $\omega_z$  on surfaces at  $Re = 200$  (same descriptions of Fig. 5). In **a** and **b**, the arrows near  $z = 0$  denote the originally generated streamwise vorticity and the vertical vorticity on the upper and rear surface stretched into downside, respectively

of one sign shed in a staggered arrangement. It is consistent with the physical description in previous works [4,5]. However, the sign of primary vertical vorticity is always the same in both the upper and lower shear layers at the same spanwise position, showing vertical vortices of one sign shed in a parallel arrangement. Such feature about specific signs of  $\omega_x$  and  $\omega_y$  in (pure) mode A already appears earlier at  $t = 49$  and is always dominant in the shear layers and near wake as time passes. Meanwhile, in a whole shedding cycle, the streamwise and vertical components of vorticity are also varied periodically on cylinder surfaces, as shown in Figs. 16–19.

The evolution of Fourier mode in the present stage is also obtained. The Fourier mode of  $n = 1$  is still dominant, associated with the wavelength  $\lambda_A$ . On the cylinder surfaces, at least one group with a mode of  $n = 2$  is identified at  $t = 560.5$ , as shown in Figs. 13f and 15 and summarized in Table 3. The distribution of Fourier mode at  $t = 472$  in Fig. 13b, e is anti-symmetric to that at  $t = 307.5$  in Fig. 13a, c. Moreover, through careful comparisons between vorticity regimes for  $n = 1$  and  $n = 2$  on cylinder surfaces, the Fourier mode of  $n = 2$  is weaker in FDW, e.g. at  $t = 560.5$ , than that in IS-2, e.g. at  $t = 375$ . Furthermore, in FDW-2, the Fourier mode of  $n = 2$  only appears on the rear surface and in certain times, typically near  $t = T_0$  (or  $T_4$ ) and  $T_2$ , as shown in Figs. 17e and 19e, but disappeared at  $t = T_1$  and  $T_3$ , as shown in Figs. 16e and 18e. In summary, the subordinate Fourier mode of  $n = 2$  initially appears in IS-2 on and near the cylinder surfaces, obviously weakened on the front sur-

face in FDW, or mainly existing on the rear surface in a certain time of FDW stage.

However, the symmetry of surface vorticities ( $\omega_x$  and  $\omega_y$ ) could be clarified if the Fourier mode of  $n = 2$  was ignored. Such symmetry is exactly the same as that appearing in CT-4 and IS-1, particularly on the rear surface, i.e.,  $\omega_x$  with a single sign, but  $\text{sgn}(\omega_y)$  symmetrical about the pipe center at the same spanwise position. It can help us to find out the physical origin of streamwise and vertical vorticities in the shear layers.

In the present stage, considering previous conclusions before FDW, we can draw a conclusion that the first sign law in R-I is valid throughout the whole evolution of vorticity, i.e.,  $\text{sgn}(\omega_x \cdot \omega_y) = 1$  on the upper side ( $y > 0$ ) and  $-1$  on the lower side ( $y < 0$ ). It is theoretically verified based on the VIVor theory for the flow past a bluff body under the geometric disturbance [19]. It should be pointed out that the effect of upstream geometric disturbance is persistent and strong enough to undergo the downstream convection of inertial forces, while the natural 3-D perturbation in the flow past the straight cylinder is random, unstable and unsustainable to be convected upstream and finally only convected downstream under same effect of inertial forces. As a result, only the first sign law downstream in the previous work [19] is valid here.

Furthermore, in R-II and R-III, it is also found that the first sign law obtained above is still effective. This not only agrees well with previous conclusions before FDW, but is also consistent with the theoretical result for downstream



regions [19]. This also indicates that the first sign law in R-II and R-III is irrelevant to time progression.

Based on the above analysis, we are certain that the second sign law, i.e.,  $\text{sgn}(\omega_x \cdot \omega_y \cdot \omega_z) = -1$ , prevails very precisely in R-I and R-II for dominant vorticity. Although there is a problem with the convective and stretching effects of inertial forces on  $\omega_x$  and  $\omega_y$  as stated in previous analysis in IS-2, the sign relationship among them is also theoretically valid for the shedding mode A, just because it stems from the shear layers.

### 3.3 Physical origin of $\omega_x$ and $\omega_y$ in the shear layers

#### 3.3.1 In the computational transition

The physical origin of  $\omega_x$  and  $\omega_y$  in the shear layers at the same spanwise position in the computational transition is analyzed. In the upper shear layer in CT-2, the sign of  $\omega_x$  is the same as that on the rear surface, e.g. in Fig. 5a, d, which indicates that  $\omega_x$  could originate from that on the rear surface, similar to previous results [21,22]. However, as shown in Fig. 5b, e, the different signs of  $\omega_y$  on the rear surface and in the upper shear layer show that  $\omega_y$  does not originate from that on the rear surface. These phenomena are also valid in CT-3. But it is not always the same in CT-4. For example, at  $t = 49$ ,  $-|\omega_x|$  in the upper shear layer could originate from that on the upper surface due to the same sign of  $\omega_x$ , but  $+|\omega_x|$  initially appearing and accumulating in the lower shear layer certainly does not originate from that on the lower surface because of an opposite sign, as shown in Figs. 9a, d and 10a. It is referred to as the paradox of origin of  $\omega_x$  in the (pure) mode A. As for the origin of  $\omega_y$  in the upper shear layer, as shown in Figs. 9b, e and 10b, it is found that  $\omega_y$  actually originates from that on the lower and rear surface, as indicated by the arrow with a hollow head in Fig. 10b, stretched by spanwise vortex in the upper shear layer.

#### 3.3.2 In the initial stage and the first stage of FDW

The origin of  $\omega_x$  in the shear layers is firstly analyzed. As an example, the spanwise position near  $z = 0$  is discussed as follows. At  $t = 375$ , the above paradox of the origin of  $\omega_x$  in CT still exists, as shown in Figs. 12a, d and 13d, similar to that at  $t = 49$  or 173 ( $T_2$ ). Interestingly, it is also confirmed that a similar situation appears at  $t = 560.5$  ( $T_0$ ), as shown in Fig. 15 or 20a. Consequently, it could be inferred that only  $-|\omega_x|$  in the upper shear layer stems from that on the upper and rear surface, associated with the formation of negative spanwise vortex, for  $T_2$  and similarly for  $T_0$ . This mechanism is well consistent with Yokoi and Kamemoto's works [21,22]. However, it is invalid in Fig. 14a indicated by the arrow, denoted as the streamwise vorticity in the lower shear layer "VorX0\_D", for  $T_2$  or in an inverse case of Fig. 20a indicated

by the arrow, denoted as the streamwise vorticity in the upper shear layer "VorX0\_U", for  $T_0$ .

Therefore, the formation and shedding process of streamwise vorticity in the shear layers can be analyzed according to Figs. 14a and 20a. At  $T_0$ , the streamwise vorticity "VorX0\_U" is firstly generated in the upper shear layer. Then when the time proceeds to  $T_2$ , "VorX0\_U" is accumulated into "VorX1\_U" in the upper shear layer. Meanwhile, "VorX0\_D" is generated in the lower shear layer. At last for  $T_0$ , "VorX1\_U" in the upper shear layer is about to be shed associated with the new "VorX0\_U" initially generated adjacent to the body. At the meantime, the enhanced "VorX0\_D" becomes "VorX1\_D" in the lower shear layer. Based on analysis of such process, there must be a new physical mechanism responsible for the initially generated streamwise vorticity close to the body, such as "VorX0\_U" or "VorX0\_D", rather than the previous mechanism only stemmed from the rear surface.

The origin of  $\omega_y$  in the shear layers is simply analyzed. At  $t = 375$ ,  $-|\omega_y|$  in the upper shear layer dominantly originates from that generated on the lower and rear surface, as shown in Fig. 12b, stretched by  $-|\omega_z|$ , similar to that appeared in Fig. 10b at  $t = 49$ . Considering Fig. 11b, this mechanism is valid at  $T_2$ . Meanwhile, at  $T_0$ , a similar mechanism,  $-|\omega_y|$  in the lower shear layer originating from that on the upper and rear surface prevails, as shown in Fig. 15b indicated by the arrow with a hollow head near  $z = 0$ , or as shown in Fig. 20b. Resultantly, it can be drawn a conclusion that the vertical vorticity in the upper or lower shear layer actually originates from that on the rear and lower or upper surface, respectively.

#### 3.3.3 In the second stage of FDW

In the second stage of FDW, by presenting a whole cycle of (pure) mode A, the analysis of the origin of  $\omega_x$  in the shear layers is then performed as follows, considering special symmetry of surface vorticity mentioned above. As stated in the above analysis, the problem of origin of  $\omega_x$  always exists in the shedding mode A. As shown in Figs. 21a or 22a, it is theoretically confirmed based on the VIVor theory and the first sign law [19] that  $+|\omega_x|$  in "VorX0\_D" or  $-|\omega_x|$  in "VorX0\_U" is actually induced by  $-|\omega_y|$  on the lower or upper and rear surface, respectively, as shown in Figs. 21b or 22b. Interestingly, this new mechanism, referred as to the vortex-induced vortex mechanism, is very similar to that observed in mode A of a square cylinder [23]. It is also examined that "VorX0\_D" initially appears at an earlier time  $T_S$  (as shown in Fig. 4) between  $T_0$  and  $T_1$ , while "VorX0\_U" at  $T_E \in (T_2, T_3)$ , e.g.  $871 < T_S < 871.5$  here. Consequently, the following formation process of  $+|\omega_x|$  in the lower shear layer near  $z = 0$  is obtained:

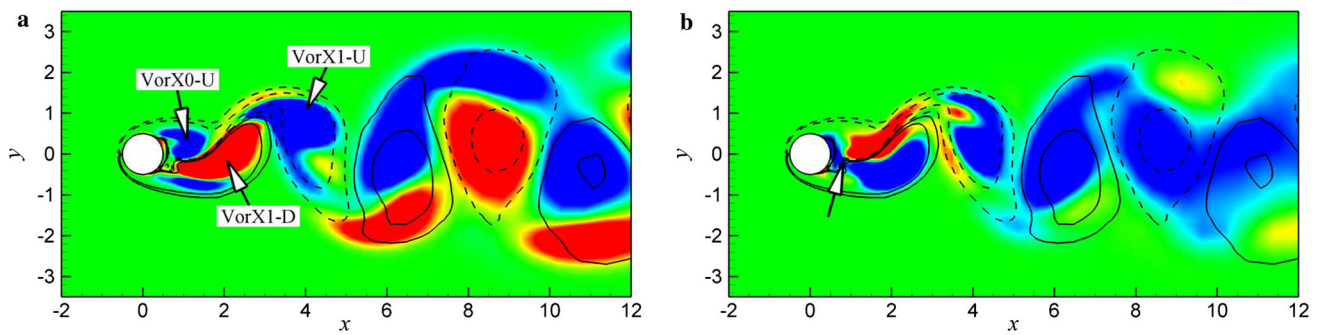


**Fig. 20** Colorful contours of **a**  $\omega_x$  and **b**  $\omega_y$  at  $z = 0.5$ ,  $t = 560.5$  (FDW-1,  $T_0$ ) and  $Re = 200$  (same descriptions as Fig. 10). In **b**, the arrow with a hollow head denotes  $\omega_y$  in the lower shear layer actually originated from that on the upper and rear surface

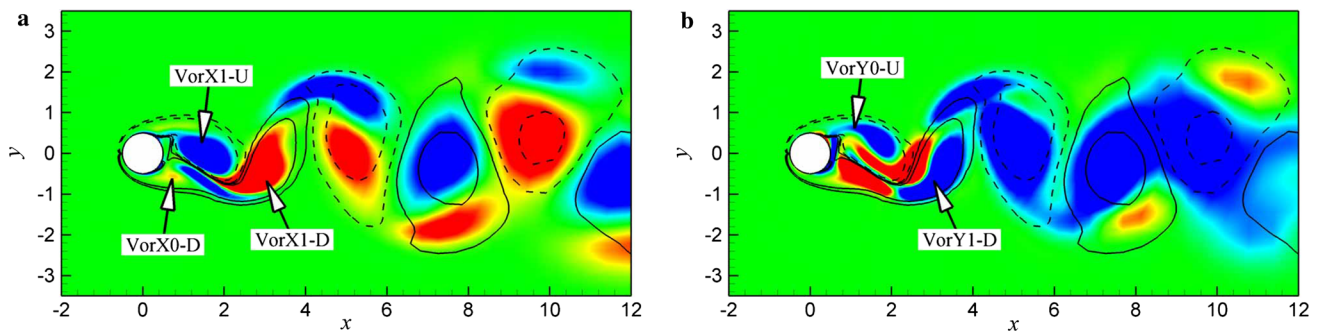


**Fig. 21** Colorful contours of **a**  $\omega_x$  and **b**  $\omega_y$  at  $z = 0.6$ ,  $t = 872$  (FDW-2,  $T_1$ ) and  $Re = 200$  (same descriptions as Fig. 10)

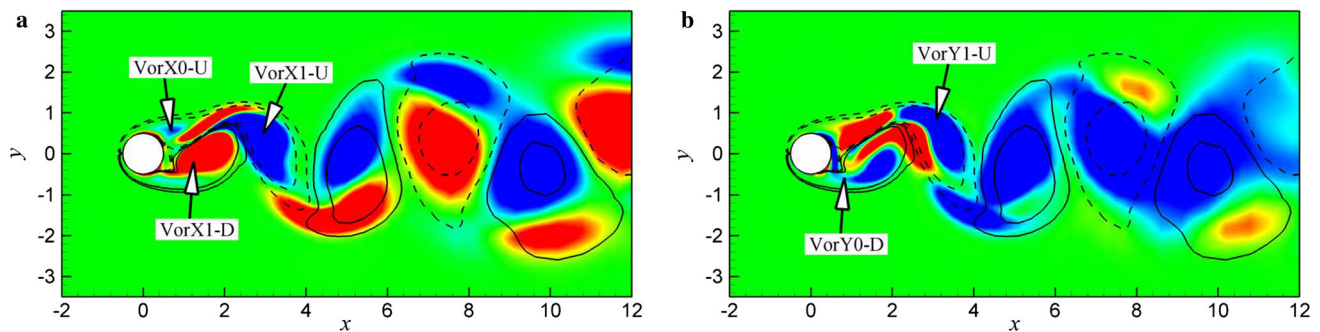


**Fig. 22** Colorful contours of **a**  $\omega_x$  and **b**  $\omega_y$  at  $z = 0.6$ ,  $t = 980$  (FDW-2,  $T_3$ ) and  $Re = 200$  (same descriptions as Fig. 10)

1.  $+|\omega_x|$  of “VorX0\_D” is firstly induced by  $-|\omega_y|$  on the lower and rear surface at  $t = T_S$ .
2. Then “VorX0\_D” is increased when time proceeds in a half-period ( $T_S, T_E$ ), as shown in Figs. 14a or 17a and 21a.
3. At  $t = T_E$ , “VorX0\_D” grows into “VorX1\_D”, as shown in Figs. 19a and 22a or Fig. 20a.
4. “VorX1\_D” thus starts to gain the streamwise vorticity not only induced by  $-|\omega_y|$  stretched from that on the upper and rear surface, but also generated on the lower and rear surface, as shown in Fig. 22a and b, in a subsequent half period ( $T_E, T_S$ ).
5. Finally at  $t = T_S$ , “VorX1\_D” is totally shed with the shedding spanwise vortex, and a new “VorX0\_D” in the

lower shear layer is induced by the vortex-induced vortex mechanism.

Correspondingly, the formation process of  $-|\omega_x|$  in the upper shear layer is just opposite to that of  $+|\omega_x|$  above, i.e., “VorX0\_U” induced in ( $T_E, T_S$ ) and “VorX1\_U” grown in ( $T_S, T_E$ ). Therefore, such process clearly illustrates that the origin of streamwise vortices is firstly as a result of vortex-induced vortex mechanism, and then the coupled mechanism with the vorticity generated on the cylinder surface [21,22]. By the way, such vortex-induction mechanism can also explain the generation of vertical vorticity in the upper shear layer in Figs. 5b or 6b, i.e.,  $\pm|\omega_y|$  induced by  $\pm|\omega_x|$  originating from those on the upper and rear surface, respectively.

**Table 4** Summary of formation and shedding process of streamwise and vertical vorticities in the upper ( $y > 0$ ) and lower ( $y < 0$ ) shear layers in a whole cycle of (pure) mode A, associated with alternately shedding spanwise vortices with vorticity  $\pm|\omega_z|$ , at  $Re = 200$ 

Time		
	$T_S$	$T_S \rightarrow T_1 \rightarrow T_2 \rightarrow T_E$
$y > 0$	VorX0_U $\mapsto$ VorX1_U	VorX1_U(In)
	VorY0_U(Ap)	VorY0_U(In)
	$- \omega_z $ (In)	$- \omega_z $ (In)
$y < 0$	VorX0_D(Ap), VorX1_D(Sh)	VorX0_D(In), VorX1_D(Sh)
	VorY0_D $\mapsto$ VorY1_D	VorY1_D(Sh)
	$+ \omega_z $ (Sh)	$+ \omega_z $ (Sh)
Time		
	$T_E$	$T_E \rightarrow T_3 \rightarrow T_4 \rightarrow T_S$
$y > 0$	VorX0_U(Ap), VorX1_U(Sh)	VorX0_U(In), VorX1_U(Sh)
	VorY0_U $\mapsto$ VorY1_U	VorY1_U(Sh)
	$- \omega_z $ (Sh)	$- \omega_z $ (Sh)
$y < 0$	VorX0_D $\mapsto$ VorX1_D	VorX1_D(In)
	VorY0_D(Ap)	VorY0_D(In)
	$+ \omega_z $ (In)	$+ \omega_z $ (In)

“Ap”, “In” and “Sh” in brackets denote the vorticity initially appearing, increasing and shed, respectively, and symbol  $\mapsto$  indicates the transformed or evolved process

This mechanism is obviously different from previous mechanisms occurring in the shear layers and near wake, e.g. the deformation of primary vortices due to an elliptic instability of the shedding primary vortex cores and coupled effect of Biot–Savart induction [2,4,5,14,24,25], the model of vortex tongues in the vortex sheet [26], and an axial stretching of the upstream perturbed vorticity, existing on the braids, due to the strain field created by the spanwise vortices which evolve under a shear instability of the wake [27].

The origin of  $\omega_y$  in the shear layers is also presented in brief. Further verified by the arrow for vertical vorticity in the upper shear layer “VorY0\_U” in Fig. 21b as the origin of  $\omega_y$  in the upper shear layer, i.e., “VorY1\_U”, is only stretched from that generated on the lower and rear surface during a half-cycle ( $T_S$ ,  $T_E$ ). Similarly for vertical vorticity in the lower shear layer “VorY0\_D”, the origin of “VorY1\_D” is generated on the upper and rear surface in another half-cycle ( $T_E$ ,  $T_S$ ) in Fig. 22b. This is exactly the same as that mentioned above.

### 3.4 Pure mode A: redescription, formation and whole shedding process

From the point of vorticity with specific sign, the (pure) mode A can be redescribed. In the near wake, typically, as shown in Fig. 17, according to the vortex structure of mode A and the second sign law described above in the near

wake, we can define the  $\Pi_-$  vortex with three components and specific signs,  $(+|\omega_x|, +|\omega_y|, -|\omega_z|)$  at  $z = \frac{1}{4}\lambda$  and  $(-|\omega_x|, -|\omega_y|, -|\omega_z|)$  at  $z = \frac{3}{4}\lambda$ , shed from the upper shear layer and the  $\Pi_+$  vortex,  $(-|\omega_x|, +|\omega_y|, +|\omega_z|)$  at  $z = \frac{1}{4}\lambda$  and  $(+|\omega_x|, -|\omega_y|, +|\omega_z|)$  at  $z = \frac{3}{4}\lambda$ , shed from the lower shear layer, respectively, where  $\lambda$  is the spanwise wavelength of  $\Pi$ -type vortex. As for the  $\Pi$ -type vortex itself, also identified and appeared in the mode A of a square cylinder [23], the head line, —, denotes the spanwise vortex alternately shed from the upper or lower shear layer, while two legs, ||, denote the rib-like vortex tubes, associated with streamwise and vertical vortex pairs with opposite signs. These tubes are also alternately shed with the spanwise vortex and thus stretched or elongated into the upstream vortex braid region by the upstream spanwise vortex of opposite sign. Consequently, the (pure) mode A can be redescribed by the  $\Pi_-$  and  $\Pi_+$  vortices alternately shed in phase across the span when  $\lambda = \lambda_A$ , well consistent with that in a previous work [28].

On the basis of the above analysis, especially the origin of  $\omega_x$  and  $\omega_y$  in the shear layers, the formation and shedding process of (pure) mode A in a whole cycle can be briefly described in Table 4. This clearly demonstrates that  $\omega_x$  and  $\omega_y$  on the same side of the shear layer initially appear out of phase, but are shed in-phase along the time. The formation process, before shedding, of streamwise vorticity of one sign experiences a whole cycle, while the formation or shedding process of vertical vorticity of one sign just lasts a half-period.

### 3.5 Effect of Reynolds number on sign relationships at $Re = 190, 195$ and $210$

The effect of Reynolds number on vorticity sign relationships is briefly presented here. Typically, as shown in Figs. 23 and 24 at  $Re = 190$ , Figs. 25 and 26 at  $Re = 195$  and Figs. 27 and 28 at  $Re = 210$ , spacial distributions of three components of dominant vorticity with specific signs are qualitatively consistent with those at  $Re = 200$ . It is confirmed that two sign laws are valid mainly on the front surface, in the shear layers, and theoretically in the near wake. Moreover, the physical mechanism of generation of  $\omega_x$  and  $\omega_y$  in the shear layers is also well explained by the above vortex-induced vortex mechanism at  $Re = 200$ . Therefore, as for (pure) mode A, two sign laws and physical origin of  $\omega_x$  and  $\omega_y$ , as well as the whole formation-shedding process, are irrelevant to the Reynolds number.

### 3.6 Effect of spanwise grid size, $\Delta z = 0.05$ , on vortex evolution

In present context, the effect of spanwise grid size,  $\Delta z = 0.05$ , at  $Re = 200$  on the evolution of vortex and its sign is



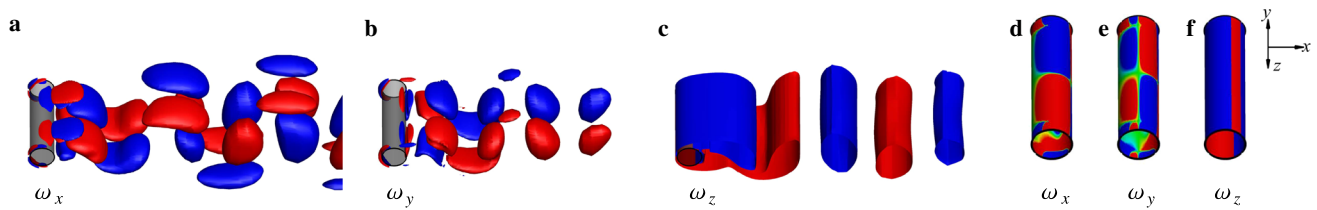


**Fig. 23** At  $Re = 190$  and  $t = 973$  ( $T_2$ ), iso-surfaces of **a**  $\omega_x = \pm 0.02$ , **b**  $\omega_y = \pm 0.02$  and **c**  $\omega_z = \pm 0.5$ , and contours of **d**  $\omega_x$ , **e**  $\omega_y$  and **f**  $\omega_z$  on surfaces (same descriptions as Fig. 5)

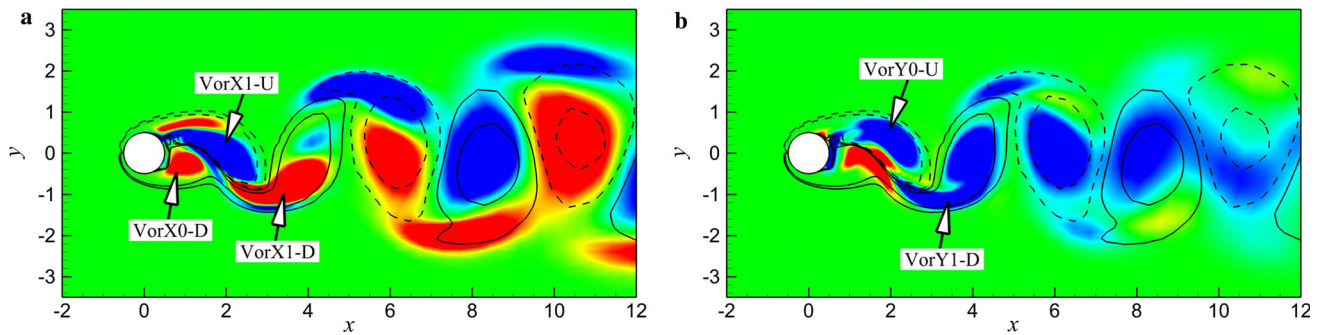


**Fig. 24** Colorful contours of **a**  $\omega_x$  and **b**  $\omega_y$  at  $z = 0.8$ ,  $t = 973$  ( $T_2$ ) and  $Re = 190$  (same descriptions of Fig. 10)

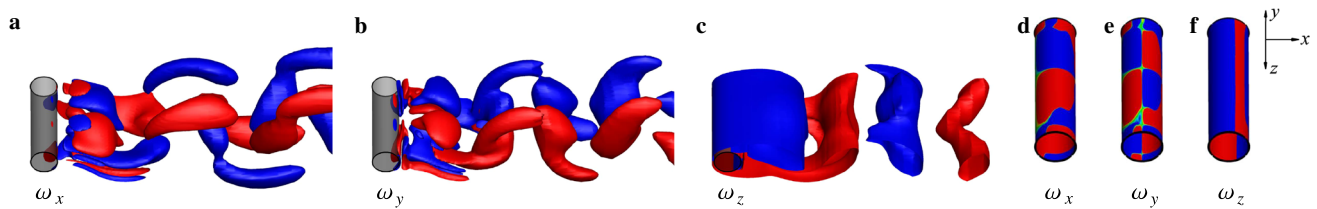


**Fig. 25** At  $Re = 195$  and  $t = 919$  ( $T_2$ ), iso-surfaces of **a**  $\omega_x = \pm 0.3$ , **b**  $\omega_y = \pm 0.2$  and **c**  $\omega_z = \pm 0.6$ , and contours of **d**  $\omega_x$ , **e**  $\omega_y$  and **f**  $\omega_z$  on surfaces (same descriptions as Fig. 5)

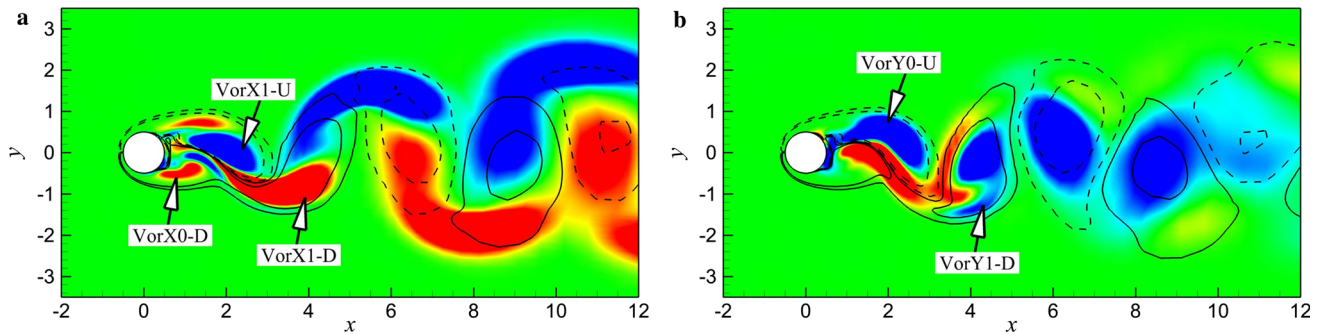


**Fig. 26** Colorful contours of **a**  $\omega_x$  at  $z = 0.6$  and **b**  $\omega_y$  at  $z = 1.2$ , at  $t = 973$  ( $T_2$ ) and  $Re = 195$  (same descriptions as Fig. 10)

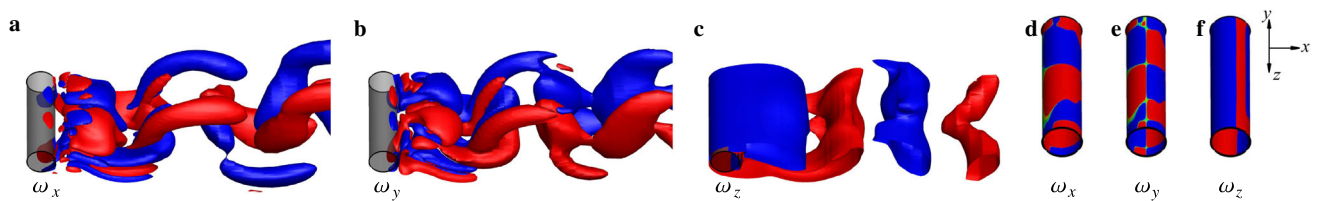


**Fig. 27** At  $Re = 210$  and  $t = 1415$  ( $T_2$ ), iso-surfaces of **a**  $\omega_x = \pm 0.3$ , **b**  $\omega_y = \pm 0.2$  and **c**  $\omega_z = \pm 0.6$ , and contours of **d**  $\omega_x$ , **e**  $\omega_y$  and **f**  $\omega_z$  on surfaces (same descriptions as Fig. 5)



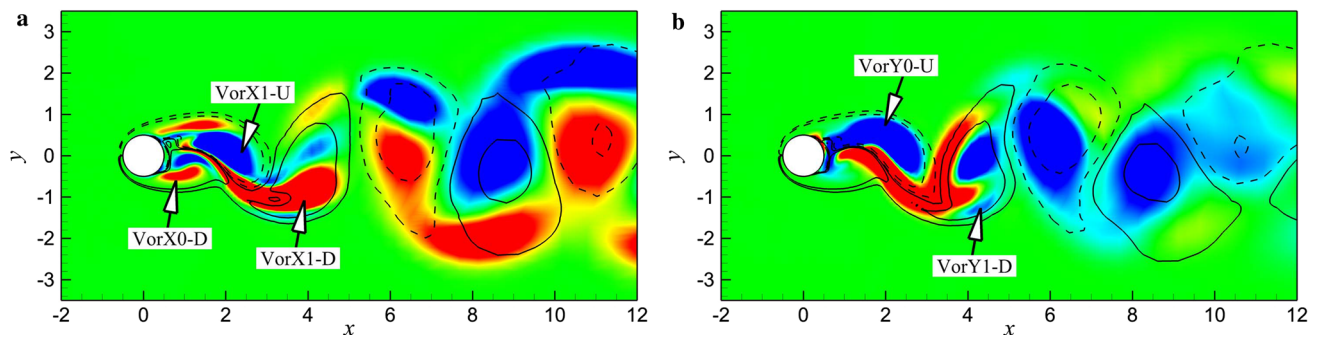


**Fig. 28** Colorful contours of **a**  $\omega_x$  at  $z = 0.8$  and **b**  $\omega_y$  at  $z = 1.2$ , at  $t = 1415 (T_2)$  and  $Re = 210$  (same descriptions as Fig. 10)

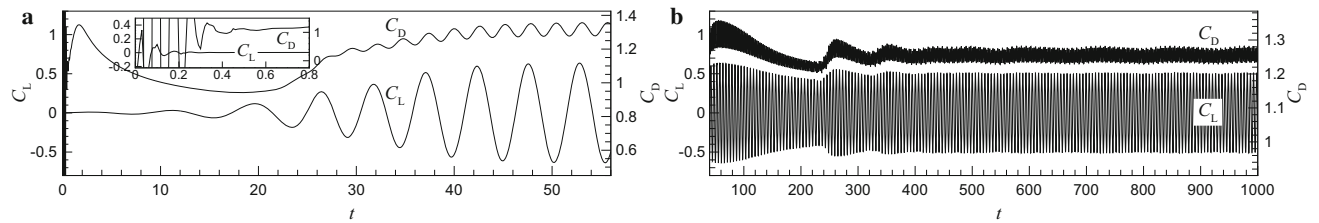


**Fig. 29** When  $\Delta z = 0.05$ , time histories of  $C_D$  and  $C_L$  for (pure) mode A at  $Re = 200$ , typically **a** the computational transition,  $t \in (0, 60)$ , with a small window at  $t < 0.8$ , **b** the initial stage,  $t \in (60, 230)$ , and the fully developed wake,  $t > 230$

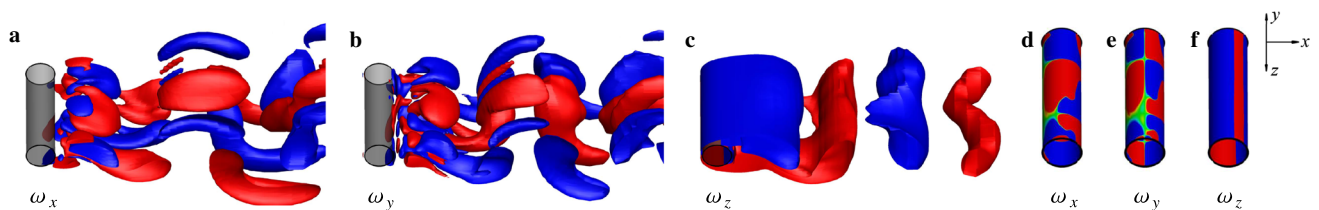


**Fig. 30** When  $\Delta z = 0.05$ , at  $Re = 200$  and  $t = 918 (T_2)$ , iso-surfaces of **a**  $\omega_x = \pm 0.3$ , **b**  $\omega_y = \pm 0.2$  and **c**  $\omega_z = \pm 0.6$ , and contours of **d**  $\omega_x$ , **e**  $\omega_y$  and **f**  $\omega_z$  on surfaces (same descriptions as Fig. 5)

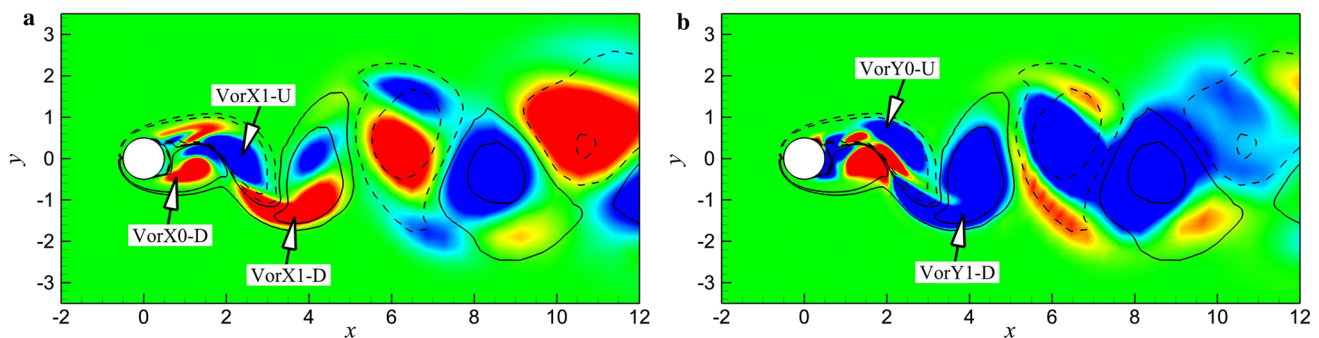


**Fig. 31** When  $\Delta z = 0.05$ , colorful contours of **a**  $\omega_x$  and **b**  $\omega_y$  at  $z = 0.8$ ,  $t = 918 (T_2)$  and  $Re = 200$  (same descriptions as Fig. 10)

also obtained. As shown in Fig. 29, it is shown that the time histories of fluid forces are qualitatively consistent with those when  $\Delta z = 0.1$ . The main difference is the time and period of every stage quantitatively. For example, the whole computational transition ends at  $t = 60$ , while the period of IS-1 from 60 to 65 is greatly reduced, almost a whole shedding period. In FDW-2 when  $t > 400$ , we have  $\overline{C_D} = 1.2552$ ,  $C'_L = 0.3569$ , and  $St = 0.1804$  with  $\delta f = 1.7 \times 10^{-3}$ , well

consistent with those when  $\Delta z = 0.1$ . However, typically, as shown in Fig. 30 at  $t = 918 (T_2)$ , sign relationships still agree well with those at  $\Delta z = 0.1$ , as well as the physical origin of  $\omega_x$  and  $\omega_y$  as shown in Fig. 31. Consequently, this means that the smaller spanwise grid size has also no qualitative effect on the evolution of vorticity and its sign, particularly for the physical origin of  $\omega_x$  and  $\omega_y$  in the shear layers.

## 4 Conclusions

The first three-dimensional wake instability, i.e., (pure) mode A, without the interference of large-scale vortex dislocation, are investigated. Direct numerical simulation for the flow past a circular cylinder is performed at a typical Reynolds number of 200 with the spanwise length equal to the most unstable instability wavelength  $\lambda_A \approx 4$ . The whole spatio-temporal evolution of vorticity is firstly presented in detail. Three objects are mainly concerned, i.e., the appearance of additional components of vorticity, the sign relationships among three vorticity components and the key effect of vertical vorticity on the origin of streamwise and vertical vortices.

Through the analysis of time histories of drag and lift coefficients, different flow stages with distinguishing features of fluid forces are identified, mainly including the computational transition, the initial stage and the fully developed wake. Particularly, in the computational transition, the wake flow is mainly evolved from the initial still flow into 2-D spanwise vortices alternately shed. As for the initial stage, the three-dimensionality in the shedding spanwise vortices with additional components of vorticity appears and is gradually intensified, associated with the basic characteristics of mode A appearing in the fully developed wake. The power spectra analysis of lift coefficient by the Morlet wavelet also confirms the above process with the vortex-shedding frequency varied from the basic frequency  $f_0$  in the 2-D wake flow to the frequency  $f_1$  in the fully developed wake.

Generally, (pure) mode A with specific vorticity and its sign distributed in the near wake are successfully obtained in present computations. From the point of the specific signs of vorticity, mode A can be described by the streamwise vorticities with opposite signs in the staggered arrangement and the vertical vortices with the same sign parallel to each other along the streamwise direction between two neighboring vortex braids associated with alternately shedding spanwise vortices with opposite signs. From the point of evolution of Fourier mode, the Fourier mode of  $n = 1$  with wavelengths of mode A is dominant in the whole flow regime after the second stage of computational transition. Particularly, other Fourier modes appear, such as  $n = 4$  only appearing in the second stage of computational transition, and sometimes  $n = 2$  mainly existing on cylinder surfaces from the second initial stage.

The spatio-temporal evolution of vorticity in mode A shows that additional vorticities appear almost throughout the whole computational time. In general along the time, they firstly appear much earlier than those in the initial stage and are gradually enhanced into a certain level in the fully developed wake. In spacial distribution, these additional vorticities initially appear on cylinder surfaces due to the intrinsic 3-D instability, which confirms that three-dimensionality of the present flow firstly occurs near solid walls, instead of the

shear layers or near wake. However, as illustrated by iso-surfaces of spanwise vorticity, these additional vorticities with magnitudes less than about 0.1 are too weak to disturb almost 2-D wake at early stage. Once they are increased up to about 0.1–0.2, obviously wavy undulation along the spanwise direction in the shedding spanwise vortices and the shear layers is observed.

Two types of symmetry of surface vorticity (except the near wake center  $y = 0$ ) at same spanwise position are discovered in different stages. The first symmetry appeared in the third sub-stage of computational transition shows signs of  $\omega_x$  on the upper and lower surfaces are opposite, as well as signs of  $\omega_y$  on the front and rear surfaces. The second symmetry existing mainly in the fully developed wake indicates that  $\omega_x$  has a single sign, but the sign of  $\omega_y$  is symmetrical about the pipe center, when only the main Fourier mode of  $n = 1$  is considered.

Based on careful comparisons among signs of three components of vorticity distributed in three sub-regions, i.e., the front surface of cylinder R-I, the shear layers R-II and near wake R-III at different times, two sign laws are summarized in present (pure) mode A for the flow past the straight circular cylinder. The first sign law shows the intrinsic relationship between  $\omega_x$  and  $\omega_y$ , precisely in region R-I and dominantly in regions R-II and R-III, written as

$$\text{sgn}(\omega_x \cdot \omega_y) = \begin{cases} -1, & \text{if } y < 0, \\ 1, & \text{if } y > 0. \end{cases} \quad (7)$$

The second sign law indicates the sign relationship between additional vorticities and spanwise vorticity, also exactly in R-I, dominantly in R-II and theoretically in R-III, written as

$$\text{sgn}(\omega_x \cdot \omega_y \cdot \omega_z) = -1. \quad (8)$$

These two sign laws are irrelevant to Fourier mode or spanwise wavelength of instability and flow stages, even in the computational transition or the initial stage. Furthermore, they are also theoretically verified by the theory of vortex-induced vortex for the flow past a bluff body under the geometric disturbance, particularly adopting results in the downstream region [19]. In addition, based on the second sign law above, (pure) mode A can be described by the  $\Pi_-$  and  $\Pi_+$  vortices with specific combinations of three components of vorticity alternately shed in phase across the span when  $\lambda = \lambda_A$ .

Furthermore, the effect of vertical vorticity in the present wake flow plays a key role. It is almost ignored and less reported in previous literature. The most important effect reveals the physical mechanism responsible for the origin of streamwise vortices in mode A. In the first half-period, the streamwise vorticity on one side of the shear layer is initially induced by the vertical vorticity on the same side and

rear surface through the vortex-induced vortex mechanism. Then in the second half-period, the coupled mechanism with the vorticity generated on solid walls is activated during the intensification of streamwise vorticity until the streamwise vortex is formed and shed with the shedding spanwise vortex. Meanwhile, the vertical vorticity in the upper or lower shear layer is always originated from that on the lower or upper and rear surface, respectively. Therefore, during the whole shedding cycle, the streamwise and vertical components of vorticity on the same side of shear layer initially appear out of phase but shed in phase along the time, as a new inherent feature found out in (pure) mode A.

Additionally, at different Reynolds numbers in the (pure) mode A, such as  $Re = 190, 195$  and  $210$ , the above sign laws and physical origin of streamwise and vertical vorticities still prevail. It is also confirmed that the effect of smaller grid size ( $\Delta z = 0.05$ ) has no effect on these physical features qualitatively.

In the future, as subsequent parts of study, the spatio-temporal evolutions of vorticity in (pure) mode B and large-scale vortex dislocation will be investigated, also mainly from present three aspects. Moreover, the effect of different spanwise wavelength of (pure) mode A on present relationships of vorticity sign could also be studied through present DNS.

**Acknowledgements** This work was financially supported by the Strategic Priority Research Program of the Chinese Academy of Science (Grant XDB22030101).

## References

- Karniadakis, G.E., Triantafyllou, G.S.: Three-dimensional dynamics and transition to turbulence in the wake of bluff bodies. *J. Fluid Mech.* **238**, 1–30 (1992)
- Wu, Z.B., Ling, G.C.: Numerical study on the mechanism for three-dimensional evolution of vortex and the structural features in the wake behind a circular cylinder. *Acta Mech. Sin.* **9**, 264–275 (1993)
- Barkley, D., Henderson, R.D.: Three-dimensional Floquet stability analysis of the wake of a circular cylinder. *J. Fluid Mech.* **322**, 215–241 (1996)
- Williamson, C.H.K.: Vortex dynamics in the cylinder wake. *Annu. Rev. Fluid Mech.* **28**, 477–539 (1996)
- Williamson, C.H.K.: Three-dimensional wake transition. *J. Fluid Mech.* **328**, 345–407 (1996)
- Henderson, R.D.: Nonlinear dynamics and pattern formation in turbulent wake transition. *J. Fluid Mech.* **352**, 65–112 (1997)
- Leweke, T., Williamson, C.H.K.: Three-dimensional instabilities in wake transition. *Euro. J. Mech. B* **17**, 571–586 (1998)
- Ling, G.C., Chang, Y.: Three-dimensional stability analysis of the periodic wake behind a circular cylinder by low-dimensional Galerkin method. *Acta Mech. Sin.* **15**, 652–660 (1999)
- Barkley, D., Tuckerman, L.S., Golubitsky, M.: Bifurcation theory for three-dimensional flow in the wake of a circular cylinder. *Phys. Rev. E* **61**, 5247–5252 (2000)
- Thompson, M.C., Leweke, T., Williamson, C.H.K.: The physical mechanism of transition in bluff body wakes. *J. Fluids Struct.* **15**, 607–616 (2001)
- Posdziech, O., Grundmann, R.: Numerical simulation of the flow around an infinitely long circular cylinder in the transition regime. *Theor. Comp. Fluid Dyn.* **15**, 121–141 (2001)
- Rao, A., Thompson, M.C., Leweke, T., et al.: The flow past a circular cylinder translating at different heights above a wall. *J. Fluids Struct.* **41**, 9–21 (2013)
- Sheard, G.J., Thompson, M.C., Hourigan, K.: A coupled Landau model describing the Strouhal-Reynolds number profile of a three-dimensional circular cylinder wake. *Phys. Fluids* **15**, L68–71 (2003)
- Jiang, H., Cheng, L., Draper, S., et al.: Three-dimensional direct numerical simulation of wake transitions of a circular cylinder. *J. Fluid Mech.* **801**, 353–391 (2016)
- Jiang, H., Cheng, L., Draper, S., et al.: Prediction of the secondary wake instability of a circular cylinder with direct numerical simulation. *Comp. Fluids* **149**, 172–180 (2017)
- Meiburg, E., Lasheras, J.C.: Experimental and numerical investigation of the three-dimensional transition in plane wakes. *J. Fluid Mech.* **190**, 1–37 (1988)
- Lin, L.M., Zhong, X.F., Wu, Y.X.: Effect of perforation on flow past a conic cylinder at  $Re = 100$ : vortex-shedding pattern and force history. *Acta Mech. Sin.* **34**, 238–256 (2018)
- Lin, L.M., Zhong, X.F., Wu, Y.X.: Effect of perforation on flow past a conic cylinder at  $Re = 100$ : wavy vortex and sign laws. *Acta Mech. Sin.* **34**, 812–829 (2018)
- Lin, L.M., Shi, S.Y., Zhong, X.F., et al.: Mechanism of wavy vortex and sign laws in flow past a bluff body: vortex-induced vortex. *Acta Mech. Sin.* **35**, 1–14 (2019)
- Persillon, A., Braza, M.: Physical analysis of the transition to turbulence in the wake of a circular cylinder by three-dimensional Navier–Stokes simulation. *J. Fluid Mech.* **365**, 23–88 (1998)
- Yokoi, Y., Kamemoto, K.: Initial stage of a three-dimensional vortex structure existing in a two-dimensional boundary layer separation flow (observation of laminar boundary layer separation over a circular cylinder by flow visualization). *JSME Int. J. Ser. II* **35**, 189–195 (1992)
- Yokoi, Y., Kamemoto, K.: Initial stage of a three-dimensional vortex structure existing in a two-dimensional boundary layer separation flow (visual observation of laminar boundary layer separation over a circular cylinder from the side of a separated region). *JSME Int. J. Ser. B* **36**, 201–206 (1993)
- Lin, L.M., Shi, S.Y., Wu, Y.X.: Physical mechanism for origin of streamwise vortices in mode A of a square-section cylinder. *Acta Mech. Sin.* **35**, 411–418 (2019)
- Jiang, H.Y., Cheng, L., An, H.W.: Three-dimensional wake transition of a square cylinder. *J. Fluid Mech.* **842**, 102–127 (2018)
- Luo, S.C., Chew, Y.T., Ng, Y.T.: Characteristics of square cylinder wake transition flows. *Phys. Fluids* **15**, 2549–2559 (2003)
- Brede, M., Eckelmann, H., Rockwell, D.: On secondary vortices in the cylinder wake. *Phys. Fluids* **8**, 2117–2124 (1996)
- Agbaglah, G., Mavriplis, C.: Computational analysis of physical mechanisms at the onset of three-dimensionality in the wake of a square cylinder. *J. Fluid Mech.* **833**, 631–647 (2017)
- Lin, L.M., Shi, S.Y., Wu, Y.X.: Intrinsic relationship of vorticity between modes A and B in the wake of a bluff body. *Theor. Appl. Mech. Lett.* **8**, 320–325 (2018)